Monthly Notices
of the
ROYAL ASTRONOMICAL SOCIETY

MNRAS **548**, 1–18 (2026)
Advance Access publication 2026 March 18

https://doi.org/10.1093/mnras/stag531

MIGHTEE-H I: mass models and dark matter properties

Anastasia A. Ponomareva,[1,2★] P. E. Mancera Piña,[3] A. A. Vărăşteanu,[2] M. Glowacki,[4,5] H. Desmond,[6] M. J. Jarvis,[2,7] T. Yasin,[2] I. Heywood,[2,8,9] N. Maddox,[10] E. A. K. Adams,[11,12] M. Baes,[13] A. Gebek,[13] S. Kurapati,[11] M. Maksymowicz-Maciata,[10] K. A. Oman,[14,15] H. Pan,[2,16] I. Prandoni,[17] S. H. A. Rajohnson,[18] I. Ruffa[19] and K. Spekkens[20]

Affiliations are listed at the end of the paper

Accepted 2026 March 17. Received 2026 March 16; in original form 2025 February 6

ABSTRACT

Measuring galaxy rotation curves is critical for inferring the properties of dark-matter haloes in the Lambda cold dark matter (ΛCDM) paradigm. We present H I rotation curves and mass models for 20 galaxies from the MIGHTEE survey. Using extended H I kinematics, we construct resolved mass models that include stellar, gaseous, and dark-matter components. Stellar masses are derived using 3.6 μm imaging under fixed mass-to-light ratio ($\Upsilon_* = M/L$) assumptions and are complemented, for the first time for a H I-selected sample, by spatially resolved M/L, obtained from multiwavelength spectral energy distribution fitting. We examine the ratio of baryonic to observed rotation velocity ($V_{\rm bar}/V_{\rm obs}$) at the characteristic radius $R_{2.2}$. Adopting a fixed $\Upsilon_\star = 0.5\,M_\odot/L_\odot$ yields a clear dependence of $V_{2.2}/V_{\rm obs}$ on galaxy luminosity, while adopting $\Upsilon_\star = 0.2\,M_\odot/L_\odot$ substantially weakens this trend. In contrast, the resolved M/L analysis preserves the luminosity dependence while modifying the stellar contribution on a galaxy-by-galaxy basis, providing a more accurate representation of the underlying relation. We model the dark-matter haloes using Navarro–Frenk–White profiles and find that the different assumptions for a fixed a M/L systematically shift galaxies relative to the theoretical stellar-to-halo mass and baryonic-to-halo mass relations, while the spatially varying M/L yields the closest agreement with theoretical benchmarks within ΛCDM. We therefore demonstrate that future investigations of the dark matter properties of galaxies using rotation curves need to account for varying M/L across individual galaxy profiles and between galaxies in order to obtain accurate measurements of the dark matter, and therefore test ΛCDM.

Key words: galaxies: kinematics and dynamics – galaxies: spiral – dark matter.

1 INTRODUCTION

Since the seminal discoveries in the late 20th century, which revealed that galaxy rotation curves remain flat at large radii rather than declining as predicted by Keplerian dynamics, it has been strongly suggested that most of the mass in galaxies is not visible (A. Bosma 1978, 1981; V. C. Rubin, J. Ford & N. Thonnard 1978). This phenomenon provided compelling evidence for the existence of dark matter (DM; T. S. Albada et al. 1985; K. G. Begeman, A. H. Broeils & R. H. Sanders 1991). The study of galaxy rotation curves has since been a cornerstone in understanding the distribution of matter in disc galaxies, as well as the connection between baryons and the DM halo. Rotation curves offer direct insight into the gravitational potential of galaxies, since the observed rotation curve consists of contributions from all dynamical components: stars, gas, and DM. Therefore, studying rotation curves is critical for inferring the presence and properties of DM haloes in the Lambda cold dark matter (ΛCDM) paradigm.

Mass modelling of galaxies, which decomposes the total gravitational potential into contributions from baryonic matter (stars and gas) and DM, is a crucial tool for understanding the structure and dynamics of galaxies (W. J. G. Blok et al. 2008; T. P. K. Martinsson et al. 2013; S. Aniyan et al. 2018, 2021). By deconstructing the observed rotation curves into the individual contributions from all dynamic components, we can explore the relative contributions of different galactic components to the overall rotation curve and hence determine the properties of the DM halo (W. J. G. Blok 2010; S.-H. Oh et al. 2015; J. I. Read et al. 2016; P. E. Mancera Piña et al. 2022b). This type of mass modelling provides insights not only into the DM itself but also the processes that shape galaxy formation and evolution, such as feedback from star formation and active galactic nuclei, which can affect the distribution of both baryons and DM within the galaxy (A. Di Cintio & F. Lelli 2016; H. Katz et al. 2017; A. Marasco et al. 2020; P. E. Mancera Piña et al. 2022b).

DM halo models, such as the Navarro–Frenk–White (NFW) profile (J. F. Navarro, C. S. Frenk & S. D. M. White 1996) or feedback-modified profiles (e.g. DC14; A. Di Cintio et al. 2014 or CORENFW; J. I. Read et al. 2016; F. Allaert, G. Gentile & M. Baes 2017), are essential for simulations and theoretical models of galaxy formation and evolution. These models provide parametrized descriptions of the DM halo structure, which can

---

★ E-mail: a.ponomareva2@herts.ac.uk

then be tested against the observed rotation curves. The NFW profile, for example, predicts a cuspy halo with a steep density gradient near the centre, as derived from DM-only simulations (V. Springel et al. 2005; A. A. Klypin, S. Trujillo-Gomez & J. Primack 2011). However, observed rotation curves, especially in low-mass and low-surface-brightness galaxies, often favour DM profiles with shallower inner slopes, implying the presence of DM cores rather than cusps (W. J. G. Blok et al. 2008; S.-H. Oh et al. 2015; P. E. Mancera Piña et al. 2025). The DC14 or CORENFW model (e.g. J. I. Read et al. 2016; F. Allaert et al. 2017), which incorporates the effects of baryonic feedback processes (such as supernova-driven outflows) on DM haloes, provides a more accurate fit to the observed data in these cases (A. Di Cintio & F. Lelli 2016; H. Katz et al. 2017). These empirical models are crucial for both interpreting observations and refining the theoretical frameworks of galaxy formation. Testing these models against a broad range of galaxy types and properties allows us to assess how well they capture the complexities of galaxy evolution, and whether they are consistent with ΛCDM predictions.

Understanding the mass distribution of galaxies within their DM haloes at $z \sim 0$ is important for tracing the Universe's assembly history. Theoretical simulations that include baryonic processes, such as gas outflows and star formation, predict that DM halo structures evolve over time (A. Di Cintio et al. 2014; E. Tollet et al. 2016). By comparing mass models from observed rotation curves and established DM scaling relations, e.g. the stellar-to-halo mass relation (SHMR) with these simulations, we can evaluate their accuracy and refine our understanding of cosmic growth (H. Katz et al. 2017; L. Posti et al. 2019; A. Marasco et al. 2020; E. M. Di Teodoro et al. 2023).

To robustly measure these halo profiles, high-quality rotation curves extending into the outer regions are essential. For galactic mass distribution studies, rotation curves derived from neutral atomic hydrogen (H I) have advantages over optical or other cold gas tracers (W. J. G. Blok et al. 2008; T. P. K. Martinsson et al. 2013; F. Lelli, S. S. McGaugh & J. M. Schombert 2016), because H I discs tend to extend farther into a galaxy's outskirts than stellar discs (W. J. G. Blok et al. 2008; G. Heald et al. 2011). This extensive spatial coverage allows for the mapping of rotational velocities to a larger radii, providing critical insights into the mass distribution where DM dominates the gravitational potential over baryons (A. Bosma 1978). Furthermore, H I is dynamically cold with a velocity dispersion of $\sigma_v \sim 10\,\mathrm{km\,s^{-1}}$ (R. Ianjamasimanana et al. 2015; K. M. Mogotsi et al. 2016; P. E. Mancera Piña et al. 2025) and follows nearly circular orbits, making it ideal for reliably tracing the total gravitational potential (G. Iorio et al. 2017; P. E. Mancera Piña et al. 2021). In contrast, optical and CO tracers are confined to the inner regions due to the much more compact distribution of stars and molecular gas, resulting in a less comprehensive view of a galaxy's mass profile, and tend to be more susceptible to the mass modelling degeneracy, such as e.g. disc–halo degeneracy (W. J. G. Blok et al. 2016; B. S. Frank et al. 2016; F. Combes et al. 2019; B. Balmaverde et al. 2021; G. Venturi et al. 2021). These advantages make H I rotation curves an indispensable tool for accurate mass modelling in galactic studies.

A significant challenge in mass modelling of observed rotation curves arises from the disc–halo degeneracy, where the contributions of the stellar disc and DM halo to the overall gravitational potential can be difficult to disentangle. This degeneracy arises from the difficulty to accurately determine the mass of the stellar disc, particularly since both the disc and halo influence the shape of the rotation curve (M. A. Bershady et al. 2010; S. Aniyan et al. 2018, 2021). Methods to address this issue include using stellar population synthesis models to estimate the mass-to-light ratio (Υ_*) of the stellar disc (J. Schombert, S. McGaugh & F. Lelli 2019, 2022), or applying the maximum or minimum disc hypotheses, which assume that the disc contributes the maximum or minimum amount of mass allowable by the observed rotation curve. Additionally, other techniques, such as measuring the vertical velocity dispersion of stars in the disc, can provide further constraints to break the degeneracy (M. A. Bershady et al. 2010; T. P. K. Martinsson et al. 2013; S. Aniyan et al. 2018, 2021).

In this paper, we present resolved H I rotation curves for a sample of 20 galaxies selected from the MeerKAT International GigaHertz Tiered Extragalactic Exploration (MIGHTEE) H IData Release (DR) 1 (I. Heywood et al. 2024) and utilizing L2 band spanning a period of approximately one billion years in lookback time ($0 < z < 0.08$). By combining H I observations with ancillary Spitzer photometry and resolved stellar mass surface densities from A. A. Vărăşteanu et al. (2025), we construct detailed mass models to disentangle the contributions of stars, gas, and DM in each system. We investigate how different assumptions about stellar mass measurement affect the inferred baryon-to-total dynamic mass relation. We further compare the derived DM halo properties and scaling relations, such as the stellar-to-halo and baryonic-to-halo mass relations (BHMRs), against theoretical predictions from abundance matching (AM) and hydrodynamic cosmological simulations.

This paper is organized as follows. Section 2 describes the latest MIGHTEE-H I data release and the H I data utilized in this study. Section 3 explains the derivation of H I rotation curves and surface mass density profiles. Section 4 outlines the method used to obtain stellar brightness profiles. Section 5 presents the constructed mass models and examines the impact of different stellar mass measurements. Section 6 discusses the properties of DM and associated scaling relations. Finally, the summary and conclusions, as well as avenues for future work are presented in Section 7.

Throughout the paper we assume a ΛCDM cosmology parameters of $H_0 = 67.4\,\mathrm{km\,s^{-1}\,Mpc^{-1}}$, $\Omega_\mathrm{m} = 0.315$, and $\Omega_\Lambda = 0.685$ (Planck Collaboration VI 2020), and adopt standard values for the critical density ($\rho_\mathrm{crit} = 1.36 \times 10^{11}\,M_\odot\,\mathrm{kpc^{-3}}$) and gravitational constant ($G = 4.3009 \times 10^{-6}\,\mathrm{kpc}\,M_\odot^{-1}\,\mathrm{km^2\,s^{-2}}$).

2 H I DATA

MIGHTEE is a survey of four well-known deep extragalactic fields observed by MeerKAT, the SKA precursor radio interferometer located in South Africa (J. L. Jonas 2009). MeerKAT consists of 64 offset Gregorian dishes (13.5 m diameter main reflector and 3.8 m sub-reflector) and is equipped with three receivers: UHF band (MHz $580 < \nu < 1015$ MHz), L band (MHz $900 < \nu < 1670$ MHz), and S band (MHz $1750 < \nu < 3500$ MHz). The MeerKAT data are collected in spectral mode, making MIGHTEE a spectral line, continuum, and polarization survey (M. Jarvis et al. 2016). The H I emission project within the MIGHTEE survey (MIGHTEE–H I) is described in detail in N. Maddox et al. (2021).

The Early Science (ES) MIGHTEE–H I data have resulted in various publications and discoveries (e.g. S. Ranchod et al. 2021; M. N. Tudorache et al. 2022), with the source catalogue released in A. A. Ponomareva et al. (2023). For this study, we utilize the DR1 H I data from the deep MIGHTEE spectral line observations of the COSMOS field (I. Heywood et al. 2024). These data are deeper and cover a larger area of the COSMOS field than the ES

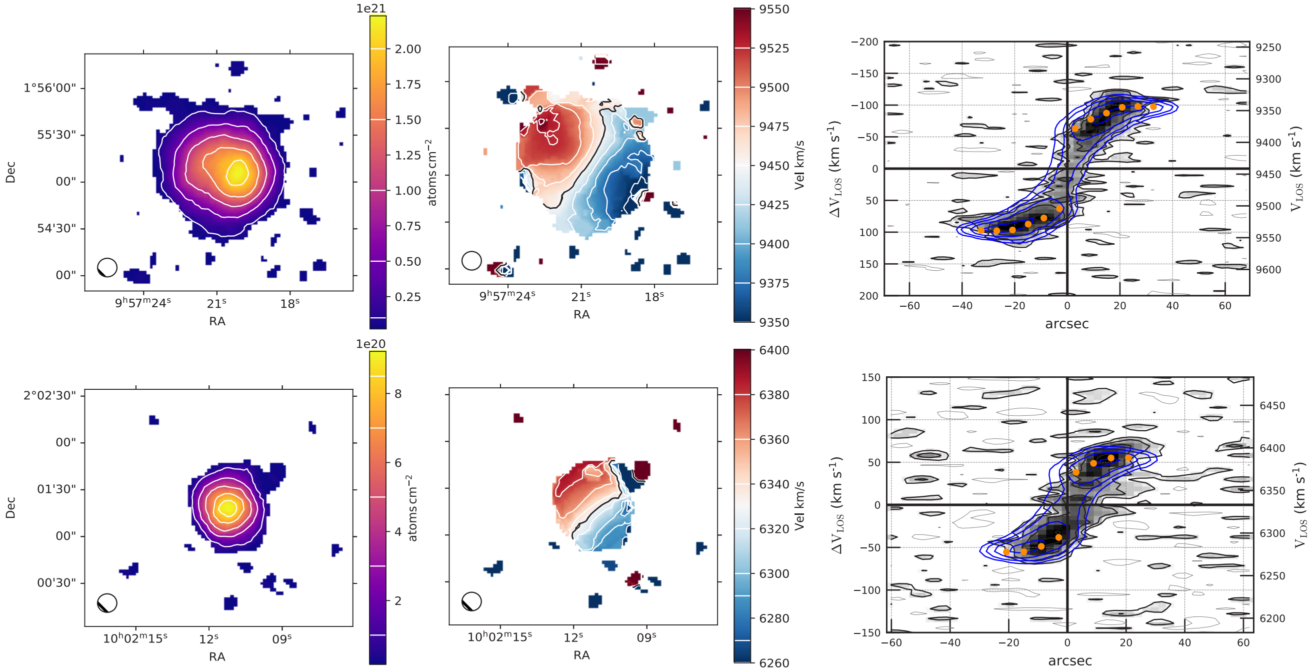

Figure 1. H I moment maps and PV diagrams for two representative galaxies, J095720.6+015507 (top) and J100211.2+020118 (bottom). The left panel shows the H I moment-0 map, the central panel the moment-1 map, and the right panel the PV diagram along the major axis, with the derived line-of-sight rotation curve (orange) and model (blue) overplotted. The synthesized beam is shown as an ellipse in the lower left corner.

data, with a total of 94.2 h on-target and a close-packed mosaic of 15 individual pointings (covering $> 4\,\mathrm{deg}^2$ on the sky). The spectral imaging covers two broad regions (960–1150 MHz and 1290–1520 MHz) within MeerKAT's *L* band, with up to 26 kHz (5,5 km s^{-1}) spectral resolution, in contrast to the ES data with coarser velocity resolution of 208 kHz (44 km s^{-1}) at $z = 0$ (A. A. Ponomareva et al. 2021).

The data were processed to produce constituent images for mosaics constructed from all pointings at three different resolutions. For this study, we utilize the highest spatial resolution to ensure our galaxies are sufficiently resolved for the 3D kinematic modelling. The typical angular resolution for our data is 12 arcsec with a circular synthesized beam and a velocity resolution of 5.5 km s^{-1} at $z = 0$. The median noise in the highest spectral resolution data (5.5 km s^{-1} at $z = 0$) is 74 μJy beam^{-1} channel^{-1}, corresponding to a 3σ H I column density sensitivity ($N_{H\,I}$) of 9×10^{18} cm^{-2}. For a full description of the data processing, analysis, and release, see I. Heywood et al. (2024).

2.1 The sample

For this study, we rely on the H Isource catalogue from the MIGHTEE early science (ES) data covering the COSMOS field (A. A. Ponomareva et al. 2023). All 75 galaxies identified in the ES data have been recovered in the DR1 (I. Heywood et al. 2024). At this stage we do not perform any additional source finding.

Out of the 75 sources, we select galaxies that are resolved with at least three resolution elements across their major axes, as estimated using the M_{HI}–D_{HI} relation (S. H. A. Rajohnson et al. 2022), have inclinations greater than 20°, and are detected in H I with a signal-to-noise ratio exceeding 3 per channel map, ensuring reliable kinematic modelling. For a detailed description of the selection procedure for galaxies suitable for kinematic analysis, see A. A. Ponomareva et al. 2021 (section 4.3.1).

Our final sample comprises 20 galaxies spanning a wide range of circular velocities, from 40 to 200 km s^{-1}, H I masses of $10^7 \leq M_{\mathrm{HI}}[\mathrm{M}_\odot] < 10^{10}$ (I. Heywood et al. 2024), and stellar masses of $10^7 \leq M_*[\mathrm{M}_\odot] < 10^{11}$ (N. Maddox et al. 2021). The sample spans the entire redshift range of the MIGHTEE L2 band (I. Heywood et al. 2024), covering approximately 1 Gyr in lookback time ($0 \leq z \leq 0.08$). The H I data [moment 0 and moment 1 maps, as well as position–velocity (PV) diagrams extracted along the major axis] for two representative galaxies from our sample are shown in Fig. 1. The main parameters of the sample used in this work can be found in Table A1.

This sample constitutes a pilot study using the MIGHTEE–H IDR1 in the COSMOS field, showcasing the power of the MIGHTEE survey to deliver resolved H I kinematics in deep extragalactic fields up to $z \sim 0.1$. Future data releases covering the XMM–Large Scale Structure (XMMLSS), Extended Chandra Deep Field South (ECDFS), ELAIS-S1, and the MIGHTEE Fornax Survey (MFS) fields will extend this work to hundreds of resolved galaxies.

3 H I ROTATION CURVES AND SURFACE MASS DENSITY PROFILES

3.1 Rotation curves

Modern 3D kinematic modelling software is capable of constraining gas dynamics in galaxies resolved with as few as three resolution elements across their major axis and with SNR $\gtrsim 3$ (E. M. Di Teodoro & F. Fraternali 2015; P. Kamphuis et al. 2015). Moreover, unlike earlier approaches that required initial estimates of key galactic parameters, such as systemic velocity, central position, and position and inclination angles to derive a rotation curve (K. G. Begeman 1989; M. A. W. Verheijen 2001; A. A. Ponomareva, M. A. W. Verheijen & A. Bosma 2016), modern kinematic modelling

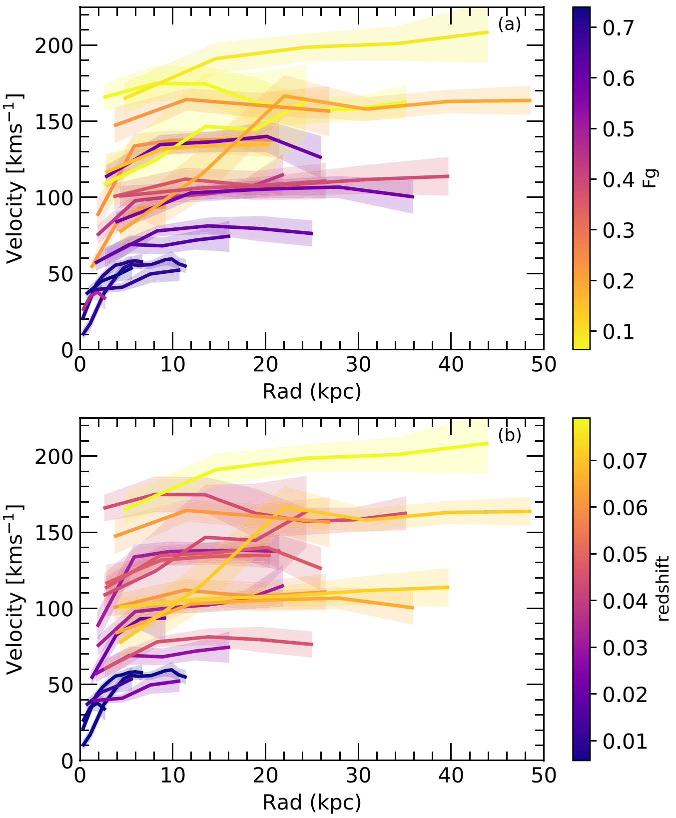

Figure 2. Rotation curves of our final sample colour-coded by the galaxies gas fraction $F_g = M_{HI}/M_{bar}$ (a) and by redshift (b). The measurement uncertainties are indicated by the shaded regions.

software is able perform fitting procedures with minimal prior information.

In A. A. Ponomareva et al. (2021), we explored the capabilities of 3DBarolo (E. M. Di Teodoro & F. Fraternali 2015) by fitting a sample of sources from the MIGHTEE ES data release in an automated way. Out of the original sample of 270 detections, only 68 presented reliable kinematic measurements suitable for resolved studies, leading to a study of the baryonic Tully–Fisher relation based on resolved kinematics. We have learned that while 3DBarolo is capable of fitting large samples of galaxies in an automated way without prior knowledge of any galaxy parameters, the inclination of galaxies remains a significant issue (P. E. Mancera Piña et al. 2020). The software performs much more reliably when an initial estimation of inclination angle is provided (see fig. 2 in A. A. Ponomareva et al. 2021).

To derive resolved rotation curves for our sample of galaxies, we use inclinations measured from the Spitzer IRAC 1 band at 3.6 μm, which is widely adopted to trace the bulk of the stellar mass distribution in galaxies (S. E. Meidt et al. 2012; M. Querejeta et al. 2015; A. A. Ponomareva et al. 2017). This near-infrared band is minimally affected by dust extinction and is largely insensitive to recent star formation, providing a robust representation of the disc geometry.

The inclinations (i) are estimated from the axis ratios using the standard relation

$$\cos^2(i) = \frac{(b/a)^2 - q_0^2}{1 - q_0^2}, \qquad (1)$$

where b and a are the semiminor and semimajor axes, respectively, and q_0 represents the intrinsic axis ratio of the disc, typically ranging between 0 (infinitely thin disc) and 0.4 (P. Fouque et al. 1990). Throughout this work, we adopt a standard value of $q_0 = 0.2$, following R. B. Tully & P. Fouque (1985).

We then use these inclinations to run 3DBarolo fully automatically, using only the data cube and the inclination as input values, keeping V_{rot} and V_{disp} as free parameters. The fully automated run adopts a ring separation equal to the beam major axis, ensuring that the kinematic measurements are largely independent and that pixel-to-pixel correlations remain negligible.[1] We set the boundary constraint for inclination fitting to $\Delta i = \pm 5^\circ$ (see A. A. Ponomareva et al. 2021 for details). To account for the uncertainties on the derived rotation curves and H I surface mass densities we utilize the built-in FLAGERRORS function in 3DBarolo, which estimates the uncertainties on the fitted parameters and the resulting rotational velocities by exploring the full parameter space, ensuring the fit converges at the minima (E. M. Di Teodoro & F. Fraternali 2015).

The resulting rotation curves for two representative galaxies from our sample are shown in Fig. 1 overplotted on top of the PV diagrams along the major axis. The compilation of all resulting rotation curves is shown in Fig. 2. Given the nature of our volume-limited untargeted survey, it is unsurprising that we predominantly detect gas-rich low-velocity galaxies at lower redshifts, whereas galaxies with higher stellar masses appear

---

[1] For consistency and to prepare for the large data load from the ongoing and upcoming H I surveys, we run the fully automated version of 3DBarolo, following the methodology and motivation detailed in A. A. Ponomareva et al. (2021).

at higher redshifts (due to larger volume probed) and exhibit lower gas fractions: $\mathrm{Fg} = 1.4M_{\rm HI}/M_{\rm bar}$, where $M_{\rm bar} = 1.4M_{\rm HI} + M_*$, with the factor 1.4 accounting for the primordial abundance of helium and metals (D. Arnett 1999). We note that our rotation curves are not corrected for pressure support (i.e. we do not apply the asymmetric drift correction, e.g. J. Binney & S. Tremaine 2008; J. I. Read et al. 2016; P. E. Mancera Piña et al. 2026). This correction is negligible for H I at our mass and rotational speed ranges, and becomes important only for galaxies $V_{\rm rot}/\sigma_v \lesssim 3$, which are typically dwarfs with $V_{\rm rot} \lesssim 20\,\mathrm{km\,s^{-1}}$ (e.g. G. Iorio et al. 2017; P. E. Mancera Piña et al. 2021).

Fig. 2 (b) shows the derived rotation curves as a function of redshift. Prior to our study, resolved H I rotation curve samples only covered galaxies up to redshift $z = 0.02$ (N. Deg et al. 2022, 2024). Although this redshift range is not expected to encompass any cosmological H I evolution (A. A. Ponomareva et al. 2021), it mitigates distance uncertainties arising from the local universe's cosmic flow and allows for cosmological luminosity distance measurements. The systemic velocities of our sample range from $V_{\rm sys} \approx 1700\,\mathrm{km\,s^{-1}}$ to $V_{\rm sys} \approx 22770\,\mathrm{km\,s^{-1}}$, with a mean value of $\bar{V}_{\rm sys} \approx 11800\,\mathrm{km\,s^{-1}}$, making the effect of peculiar velocities negligible for the majority of the sample (J. L. Tonry et al. 2000; R. B. Tully, H. M. Courtois & J. G. Sorce 2016; K. Said et al. 2020).

3.2 Gas surface mass density

Following the extraction of rotation curves, we also derive resolved radial H I surface mass density profiles taking advantage of 3DBarolo. At each radius, the mean H I flux density is estimated from the input data cubes. We then convert these values from units of flux density to physical units of H I column density, $N_{\rm HI}$ [atoms cm^{-2}], following the standard procedure (see equation 78 in M. Meyer et al. 2017). Next, we correct the column density profiles for inclination to obtain face-on values, thereby accounting for projection effects due to the galaxies' orientation. Finally, we apply the standard conversion to obtain H I surface mass density, where $1\,\mathrm{M_\odot\,pc^{-2}} = 1.249 \times 10^{20}\,\mathrm{atoms\,cm^{-2}}$.

The resulting H I surface mass density profiles are shown in Fig. 3. As expected, they exhibit a variety of shapes across our sample of galaxies. Higher mass galaxies tend to illustrate a central depletion of H I surface density, with the neutral hydrogen gas extending out to large radii. This indicates that in these galaxies, the H I gas is more distributed in the outer regions of the galactic disc. Conversely, smaller galaxies display steeper H I profiles.

4 STELLAR SURFACE BRIGHTNESS AND MASS DENSITIES

4.1 *Spitzer* photometry

The *Spitzer* IRAC 1 band at 3.6 μm is widely used to derive stellar surface brightness profiles, which are essential for subsequent mass modelling and rotation curve decomposition. One of the key advantages of the 3.6 μm wavelength is its sensitivity to the older low-mass stars that dominate the bulk of the stellar mass in galaxies. At this wavelength, the emission is not affected by dust extinction and is predominantly due to evolved stellar populations such as red giants and main-sequence stars. This results in a more accurate tracing of the underlying stellar mass distribution compared to optical wavelengths, which can be significantly influenced by recent star formation and dust obscuration (K. Sheth et al. 2010; S. E. Meidt et al. (2012).

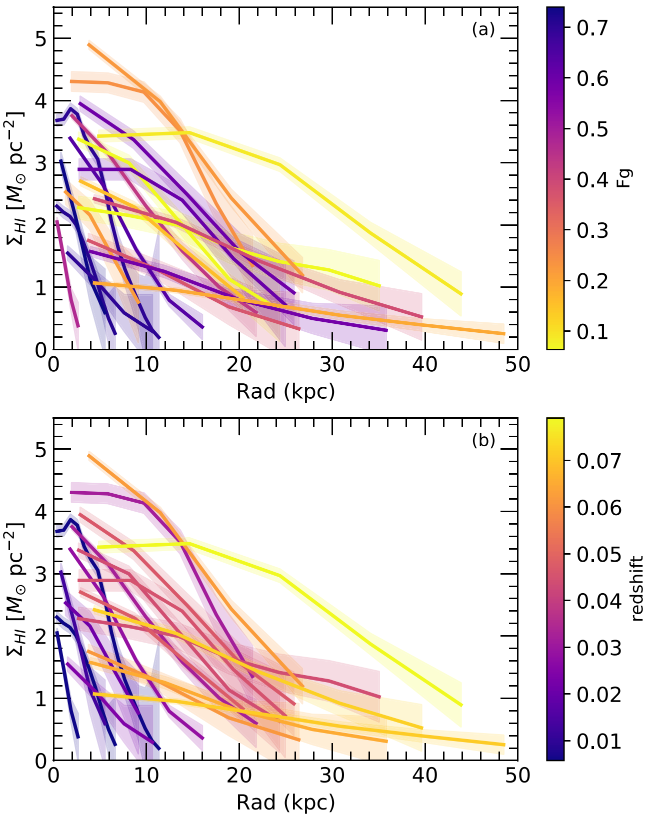

Figure 3. Inclination-corrected H I surface mass density 1D profiles of our final sample, colour-coded by the galaxies' gas fraction $\mathrm{F_g} = M_{\rm HI}/M_{\rm bar}$ (a) and by redshift (b). The measurement uncertainties are indicated by the shaded regions.

Furthermore, the stellar mass-to-light ratio (Υ_*) in the 3.6 μm band is considered to be well understood and stable across different galaxy types and stellar populations. Studies have shown that the Υ_* at 3.6 μm exhibits minimal variation with stellar population age or metallicity (B. Röck et al. 2015), allowing for a more direct and reliable conversion from observed luminosity to stellar mass (S. S. McGaugh & J. M. Schombert 2014). S. E. Meidt et al. (2014), for example, showed that the intrinsic scatter in the Υ_* ratio at 3.6 μm is less than 0.1 dex, which is significantly lower than in optical bands. A. Marasco et al. (2025) performed a comparison between stellar masses inferred from 3.6 μm data and those derived through multiwavelength spectral energy distribution (SED) modelling, demonstrating that SED fitting provides consistent stellar mass estimates in good agreement with dynamical estimates.

Additionally, the minimal impact of dust extinction at 3.6 μm reduces the need for uncertain extinction corrections, further improving the accuracy of the stellar mass profiles (M. Querejeta et al. (2015). This is particularly beneficial for edge-on galaxies or regions with high dust content, where optical observations can be severely affected. The use of 3.6 μm data thus allows for a clearer view of the stellar mass distribution, which is crucial for understanding the interplay between baryonic and DM in galaxies (A. A. Ponomareva et al. 2017, 2018). Numerous studies have successfully utilized *Spitzer* IRAC 1 band data for mass modelling and rotation curve decomposition (e.g. F. Lelli et al. 2016; S. S. McGaugh, F. Lelli & J. M. Schombert 2016; L. Posti et al. 2019; E. M. Di Teodoro et al. 2023).

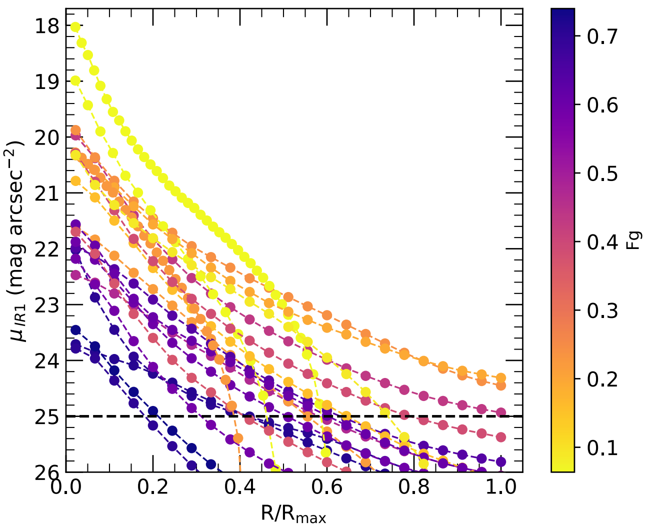

Figure 4. IRAC 1 surface brightness profiles of our final sample colour-coded by the galaxies' gas fraction, $F_g = M_{\rm HI}/M_{\rm bar}$ and normalized by the radius of the last measured ellipse ($R_{\rm max}$). The horizontal dashed line represents the *Spitzer* IRAC 1 3σ magnitude limit.

Taking all of this into account, for our study we also focus on the Spitzer 3.6 μm band to derive the stellar mass surface density for the sample galaxies. To obtain the stellar surface brightness profiles necessary for mass modelling and rotation curve decomposition, we processed the galaxy images using the standard approach (A. A. Vărăşteanu et al. 2025) and extracted the stellar surface brightness profile of each galaxy.

We defined a series of concentric elliptical annuli centred on each galaxy, with the separation between annuli set equal to the Spitzer IRAC 1 point spread function full width at half-maximum (FWHM $\sim$ 1.7 arcsec). The number of elliptical apertures was left unconstrained and extended to the edge of the image, where the background is well sampled, ensuring that the integrated light converges and the radial surface-brightness profile reaches a flat asymptotic tail. The ellipticity and position angle of the ellipses were fixed to the geometry measured using equation (1). Fixing the ellipse geometry, rather than allowing each annulus to follow the isophotal contours, has been shown to be effective for deriving surface-brightness profiles, particularly for 3.6 μm data (A. Marasco et al. 2023; B. Šiljeg et al. 2024).

Within each annulus, the mean intensity was calculated after correcting for residual background flux and applying aperture corrections. The measurement errors on the mean intensity were computed following the standard photometric error-propagation approach, in which the total variance is the sum of contributions from the object signal, sky background, and readout noise, with background noise dominating the uncertainty at faint levels (S. B. Howell 2006). The resulting surface-brightness profiles, corrected for inclination, are shown in Fig. 4 for all galaxies in the sample.

4.2 Resolved stellar mass surface densities

Owing to the limited wavelength coverage of many H I samples, 3.6 μm imaging has commonly been used as the optimal single-band proxy for stellar mass. However, within the MIGHTEE fields we have access to some of the deepest and high-quality visible (e.g. H. Aihara et al. 2018, 2019) and near-infrared (e.g. H. J. McCracken et al. 2012; M. J. Jarvis et al. 2013) imaging data available. Therefore, in addition to the stellar surface-brightness profiles derived from the *Spitzer* IRAC 1 (3.6 μm) imaging, we incorporate into our analysis the resolved stellar mass surface densities measured by A. A. Vărăşteanu et al. (2025). These were obtained through spatially resolved SED fitting across 10 optical and near-infrared bands, yielding resolved stellar mass surface-density profiles (see fig. 4 of A. A. Vărăşteanu et al. 2025).

The A. A. Vărăşteanu et al. (2025) sample is composed of the same H I-selected galaxies and overlaps with our own sample for 19 out of 20 systems. Their resolved stellar mass measurements therefore provide an independent and complementary data set that strengthens our characterization of the stellar mass distribution and its contribution to the baryonic mass budget. Spatially resolved stellar mass surface densities based on radially varying Υ_* have so far been used for mass modelling and DM inference only in a single-object study (A. Tamm et al. 2012). Here we extend this approach to a larger sample. Hereafter, we refer to these resolved stellar mass surface-density profiles as the resolved Υ_* profiles.

5 MASS MODELS

Rotation curve decomposition enables us to separate the contributions from visible and DM, offering a comprehensive picture of the overall mass structure within a galaxy. The total rotational velocity $V_{\rm tot}(R)$ at a given radius R can be expressed as the square root of the quadratic sum of the rotational velocities contributed by the various mass components of the galaxy. These components include the baryonic matter comprising gas, bulge and disc ($V_{\rm bar}$), and the DM halo ($V_{\rm halo}$):

$$V^2_{\rm tot}(R) = V^2_{\rm bar}(R) + V^2_{\rm halo}(R). \tag{2}$$

Analysing the individual contributions of these components allows us to understand the distribution of mass within each one. The gas component $V_{\rm gas}(R)$ is derived from the observed H I surface density profile (Section 3.2), while the stellar components $V_{\rm bulge}(R)$ and $V_{\rm disc}(R)$ are obtained from the surface brightness profiles (Section 4) converted to mass profiles using appropriate mass-to-light ratios. We neglect the contribution from molecular gas, which is expected to have only a minor impact on the mass modelling (B. S. Frank et al. 2016; A. A. Ponomareva et al. 2018; P. E. Mancera Piña et al. 2022b). The DM halo's contribution $V_{\rm halo}(R)$ is modelled to account for any discrepancy between the observed rotation curve (Section 3.1) and the one from the baryonic components:

$$V^2_{\rm bar}(R) = V^2_{\rm gas}(R) + V^2_{\rm stars}(R). \tag{3}$$

We construct our mass models by closely following the methodology from P. E. Mancera Piña et al. (2022a, b). To compute the gas and stellar rotation velocities, we utilize the software GALPYNAMICS,[2] which numerically calculates the gravitational potential of a given mass distribution described by a density profile as a function of radius and height above the disc mid-plane. Subsequently, GALPYNAMICS computes the circular velocity of the mass distribution by taking the derivative of the gravitational potential evaluated at the mid-plane of the mass component (see section 3.1 in P. E. Mancera Piña et al. 2022b for details).

To obtain the functional forms of the density distribution of the baryonic components of our sample galaxies, we first fit the ob-

---

[2] https://gitlab.com/iogiul/galpynamics

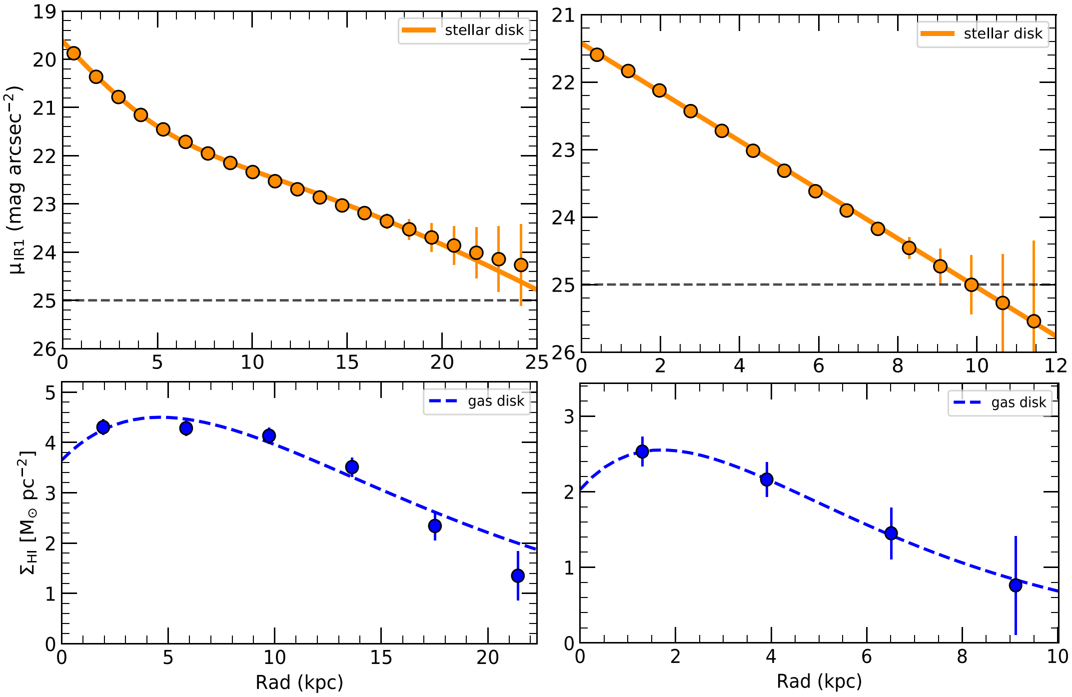

Figure 5. Surface brightness and H I gas density profiles for two representative galaxies J095720.6+015507 and J100211.2+020118 from our sample. Left column: profile for a galaxy with a pseudo bulge (orange points) described by a poly-exponential fit (orange line). The horizontal dashed line represents the 3σ magnitude limit. The bottom panel displays the radial profile of the H I gas surface density (blue points), with the dashed blue line representing the poly-exponential gas disc fit and the points indicating the observed data. Right column: profile for a galaxy without a bulge (orange points), described by exponential disc fit (line), the bottom panel shows the gas surface density profile (blue points) described by the poly-exponential gas disc fit (blue dashed line).

served H I surface mass density profiles with the poly-exponential function:

$$\Sigma_{\rm HI}(R) = \Sigma_0 \exp\left(-\frac{R}{R_d}\right)(1 + c_1 R + c_n R^n + \dots), \quad (4)$$

where Σ_0 is the central surface mass density, R_d is the exponential disc scale length, and c_1, c_2, c_n etc., are the coefficients of the polynomial. This function closely matches the surface-density profiles of gas-rich galaxies, which commonly show a central plateau or depression, rise at intermediate radii, and decline approximately exponentially at large radii (e.g. R. A. Swaters 1999; T. P. K. Martinsson et al. 2016; J. Wang et al. 2016). For complex well-resolved data, the number of polynomial coefficients can reach up to four (P. E. Mancera Piña et al. 2024). However, for our marginally resolved H I surface mass density profiles, we use only the first-degree coefficient to avoid overfitting. The resulting fits are shown in Fig. 5 (bottom panels) for two representative galaxies from our sample and demonstrate that the chosen functional form can reproduce the data, capturing the central depression common in the H I surface mass density distribution (A. A. Ponomareva et al. 2016).

Next, we model the stellar light distribution by fitting the stellar surface brightness profiles (Fig. 4) using a functional form. For galaxies with a deviation from the pure exponential disc and excess light in the centre we first model the total intensity as the sum of two components: a bulge, described by a general Sérsic profile:

$$I(R) = I_e \exp\left(-b_n\left[\left(\frac{R}{R_e}\right)^{1/n} - 1\right]\right), \quad (5)$$

where I_e is the intensity at the effective radius R_e, n is the Sérsic index, and b_n is a constant that depends on n (L. Ciotti & G. Bertin 1999), and a disc, represented by an exponential profile (a Sérsic profile with $n = 1$). We find that none of the bulges in our sample actually represent the classical bulge population, which is typically described with Sérsic index $n > 2$. Instead, we find that bulges in our sample are consistent with pseudobulges ($n \leq 2$). Pseudobulges, also known as disc-like bulges, are thought to form through the secular evolution of the galaxy's disc, driven by internal processes such as bars, spiral arms, and oval distortions (J. Kormendy & J. Kennicutt 2004). Therefore, we cannot model the dynamics of these components as purely spherical, like classical bulges. Instead, we fit our stellar profiles that exhibit this feature with a poly-exponential disc of the fourth order (equation 4; P. E. Mancera Piña et al. 2024). For pure disc systems, we fit only an exponential disc profile. Fig. 5 (upper panels) shows examples of these fits for two representative galaxies: one with a pseudobulge and another with a purely exponential disc.

To convert *Spitzer* intensities to stellar mass surface density, we use the prescription from F. Lelli et al. (2016). We apply two different values of the Υ_* for the stellar disc: the traditional value for the 3.6 μm band, $\Upsilon_* = 0.5$ (S. E. Meidt et al. 2014; J. Schombert et al. 2019) and $\Upsilon_* = 0.2$, found by T. P. K. Martinsson et al. (2013) for the discMass Survey and by A. A. Ponomareva et al. (2018) using SED modelling of disc galaxies over 18 photometric bands. In the following text, we examine how different choices of Υ_* affect the mass modelling and compare these results with those derived from spatially resolved Υ_* estimates.

We adopt the same functional forms (poly- and exponential disc) to describe the resolved Υ_* profiles from A. A. Vărăşteanu

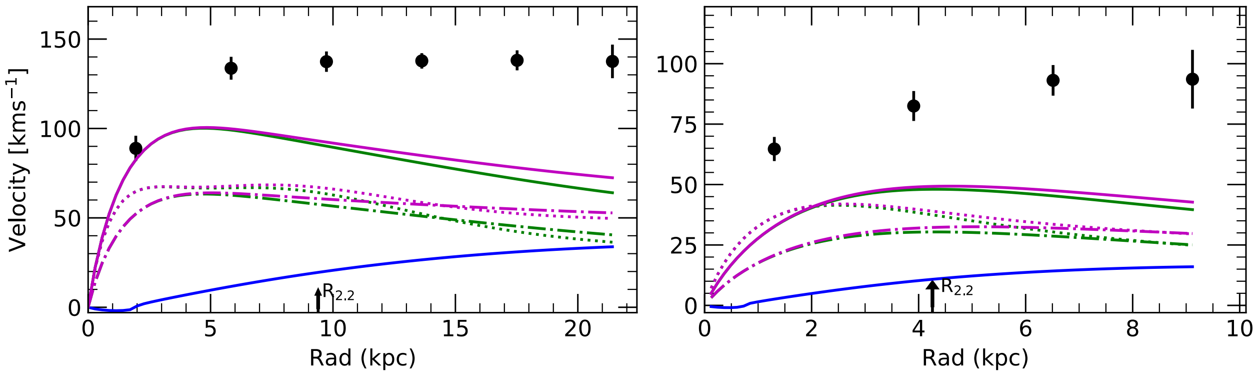

Figure 6. Baryonic mass modelling for two representative galaxies J095720.6+015507 and J100211.2+020118 from our sample. Left panel: mass modelling for the galaxy with poly-exponential disc. The observed rotation curve (black points) is compared with modelled rotational velocities from gas (blue line) and stellar disc (green line). The total baryonic rotation curve $V_{\rm bar}$ is shown with a magenta line. The solid lines represent adopted $\Upsilon_* = 0.5$, dash–dotted lines correspond to $\Upsilon_* = 0.2$, and the dotted lines correspond to the SED profiles. The arrow indicates the radius corresponding to 2.2 disc scale lengths. Right panel: baryonic mass modelling for the galaxy with pure exponential disc.

et al. (2025), who demonstrated that this form provides an adequate representation of the data.

To account for the stellar disc thicknesses, we adopt the standard assumption that the scale height of the stellar disc is $\sim 0.1R_d$ (P. Yoachim & J. J. Dalcanton 2006; S. Comerón, H. Salo & J. H. Knapen 2018). We model the vertical structure of the stellar disc using a *sech*^{2} density profile (P. C. der Kruit & K. C. Freeman 2011). For the gas disc, we assume the razor-thin approximation (A. Bosma 1981; J. Wang et al. 2016). While in reality the gas discs flare with radius (e.g. A. B. Romeo 1992; C. Bacchini et al. 2019), the dynamical effect of the flaring is only important for gas-rich dwarf galaxies with $V_{\rm rot} \lesssim 30$ km/s and $V_{\rm rot}/\sigma_v \lesssim 3$ (P. E. Mancera Piña et al. 2022b, 2025), and therefore can be neglected in our sample. Moreover, accurate computation of scale heights requires highly resolved H I observations, which are not yet attainable for samples beyond the very local universe. Therefore, we consider our approximations suitable for our sample and proceed with modelling the dynamics of the baryonic components.

Fig. 6 illustrates the baryons-only mass models for two representative galaxies from our sample, with stellar circular velocities computed from the 3.6 μm profiles assuming $\Upsilon_* = 0.5$ (solid lines) and $\Upsilon_* = 0.2$ (dash–dotted lines), and from the resolved Υ_* profiles (dotted lines). From Fig. 6, it is clear that for the galaxy with higher rotational velocity, the stellar circular velocity derived from the resolved Υ_* is closer to that obtained assuming $\Upsilon_* = 0.2$, whereas for the galaxy with lower rotational velocity it is closer to the case with $\Upsilon_* = 0.5$. This behaviour is consistent with the findings of A. A. Vărăşteanu et al. (2025), who showed that galaxies do not share a universal stellar mass-to-light ratio, and that Υ_* varies not only from galaxy to galaxy but also within individual galaxies as a function of radius (see figs 6 and 7 in A. A. Vărăşteanu et al. 2025).

An arrow indicates the radius corresponding to $2.2\times R_d$ (R$_{2.2}$) (K. C. Freeman 1970). This radius is often used for the mass modelling of galaxies since for an exponential disc, the stellar rotation curve reaches its maximum at $\sim R_{2.2}$ (T. S. Albada et al. 1985; J. Binney & S. Tremaine 2008). The ratio between the rotational velocity of the baryons and the observed rotational velocity at this characteristic radius gives a measure of the degree of the disc 'maximality' (T. P. K. Martinsson et al. 2013; N. Starkman et al. 2018). A 'maximal disc' in a spiral galaxy is commonly defined as one in which the stellar disc component contributes the largest fraction of the observed rotation curve (~ 85 per cent $\pm$ 10 per cent of the peak velocity), while leaving minimal room for a DM halo contribution (T. S. Albada & R. Sancisi 1986). Fig. 6 shows that for the first galaxy (left), $\Upsilon_* = 0.5$ produces a maximal disc, as any higher Υ_* would result in a total rotation curve exceeding the observed data. In contrast, the second galaxy (right) demonstrates greater flexibility, allowing for either a larger Υ_* or a more substantial DM contribution. Adopting $\Upsilon_* = 0.2$, on the other hand, results in the discs of both galaxies being submaximal.

5.1 The effect of the stellar mass-to-light ratio

Fig. 7 shows the ratio of the baryonic to observed rotational velocities ($V_{2.2}/V_{\rm obs}$) measured at 2.2R$_d$ for our sample galaxies, considering three different Υ_* as described in Section 5.

First, we note that our sample reproduces the same trends found by F. Lelli et al. (2016) for 175 large nearby disc galaxies (the SPARC sample). We find that the degree of disc maximality depends on the total luminosity of a galaxy when $\Upsilon_* = 0.5$ is adopted. Fig. 7 (left) demonstrates that the values of $V_{2.2}/V_{\rm obs}$ increase from approximately 0.25 for faint galaxies to nearly 1 for galaxies with higher total luminosity.

Conversely, this trend almost disappears when $\Upsilon_* = 0.2$ is adopted (Fig. 7, right), signifying little dynamical distinction between galaxies of different luminosities when a low Υ_* is assumed. However, a scenario in which all spiral galaxies have uniformly low stellar mass contributions would lead to systematic deviations from the baryonic Tully–Fisher relation (S. S. McGaugh et al. 2000) at fixed rotation velocity, which are not observed (A. A. Ponomareva et al. 2018, 2021).

Moreover, as demonstrated by A. A. Vărăşteanu et al. (2025), spatially resolved stellar mass surface densities derived from SED fitting reveal that Υ_* varies both from galaxy to galaxy and as a function of radius within individual systems. This implies that the stellar contribution to the baryonic mass distribution is neither globally uniform nor radially constant, but instead depends on the specific properties of each galaxy and location within it.

To assess how such non-universal, resolved Υ_* affects trends in fractional baryonic contribution in the inner regions, we examine

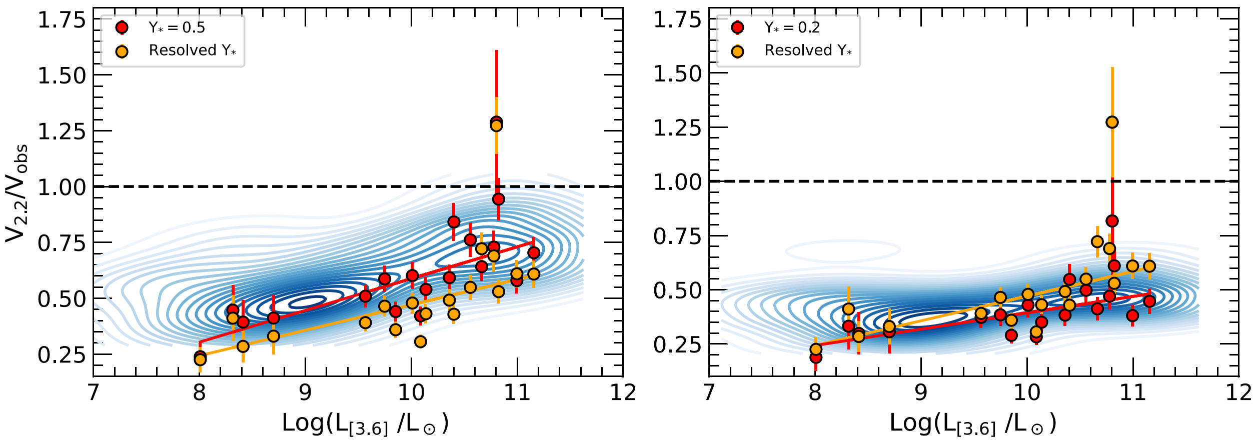

Figure 7. Ratio of the baryonic to observed rotation velocity at 2.2 disc scale lengths ($V_{2.2}/V_{\rm obs}$) as a function of the total luminosity in the 3.6 μm band for our sample galaxies (red points), shown for two adopted values of the stellar mass-to-light ratio Υ_* (Section 5). Observational trends from the SPARC data base (F. Lelli et al. 2016) are highlighted with blue regions. The dashed line represents $V_{\rm bar}/V_{obs} = 1$, which marks the upper limit for physically acceptable discs.

their impact on the $V_{2.2}/V_{\rm obs}$–luminosity relation. For this purpose, we fit a linear relation in order to quantify how the slopes of the relations change. We find that when a high stellar mass-to-light ratio ($\Upsilon_\star = 0.5$) is assumed, the ratio $V_{2.2}/V_{\rm obs}$ increases systematically with luminosity, with a slope of 0.18 ± 0.04, indicating that more luminous spiral galaxies are increasingly baryon-dominated in their inner regions. Resolved stellar mass surface densities yield a similarly strong luminosity dependence, with a slope of 0.15 ± 0.03, differing primarily in normalization (Fig. 7, orange). This demonstrates that incorporating spatially resolved stellar mass distributions preserves the physical trend of increasing inner baryonic dominance with luminosity while refining the stellar mass contribution on a galaxy-by-galaxy basis. In contrast, adopting a low stellar mass-to-light ratio ($\Upsilon_\star = 0.2$) tends to reduce the baryonic contribution at $2.2R_{\rm d}$ across the full luminosity range, leading to an almost flat relation with a slope of only 0.05 ± 0.03.

Therefore, the resolved stellar mass estimates preserve a physically meaningful $V_{2.2}/V_{\rm obs}$ dependence on luminosity, as well as alleviate the extreme form of the disc–halo degeneracy introduced by assuming a single $\Upsilon_\star$.

6 DARK MATTER PROPERTIES

Given the limited resolution of the H I rotation curves for our sample, particularly in the inner regions of the galaxies, we only focus on the standard NFW (J. F. Navarro et al. 1996) DM halo density profile. Therefore, we do not attempt to differentiate between various DM halo models and instead aim to robustly constrain the DM halo mass and assess the position of our sample galaxies with respect to established DM scaling relations. By restricting the complexity of the halo model, we ensure that the inferred parameters are physically motivated. Assuming spherical symmetry, the NFW density profile is defined as

$$\rho = \frac{4\,\rho_s}{\left(\frac{r}{r_s}\right)\left(1+\frac{r}{r_s}\right)^2}, \tag{6}$$

where r_s is a scale radius, and ρ_s is the characteristic density at r_s. The characteristic density ρ_s is related to the halo mass M_{200} and concentration c_{200} as

$$\rho_s = \frac{M_{200}}{16\pi\, r_s^3 \left[\ln(1+c_{200}) - \frac{c_{200}}{1+c_{200}}\right]}, \tag{7}$$

where M_{200} is the mass enclosed within radius R_{200}, defined such that the average density inside R_{200} is 200 $\rho_{\rm crit}$ (with $\rho_{\rm crit}$ the critical density of the Universe), and $c_{200} \equiv R_{200}/r_s$ is the concentration parameter. The enclosed mass at radius r for an NFW halo can then be expressed through the dimensionless variable $x = r/r_s$:

$$M(r) = M_{200}\,\frac{\ln(1+x) - \frac{x}{1+x}}{\ln(1+c_{200}) - \frac{c_{200}}{1+c_{200}}}. \tag{8}$$

Following the notion of spherical symmetry, the circular velocity at radius r is defined by $V_{\rm NFW}(r) = \sqrt{GM(r)/r}$. Introducing the characteristic velocity $V_{200} = \sqrt{GM_{200}/R_{200}}$, we can rewrite $V_{\rm NFW}(r)$ in terms of c_{200} and x:

$$V_{\rm NFW}(r) = V_{200}\sqrt{\frac{c_{200}}{x}}\,\frac{\sqrt{\ln(1+x) - \frac{x}{1+x}}}{\sqrt{\ln(1+c_{200}) - \frac{c_{200}}{1+c_{200}}}}. \tag{9}$$

The total (baryons and DM) circular velocity of a galaxy at each radius is then

$$V^2_{\rm tot}(R) = V^2_{\rm NFW}(R) + V^2_{\rm disc}(R) + V^2_{\rm gas}(R), \tag{10}$$

To calculate $V_{\rm tot}$ we adopt a standard Bayesian mass-modelling framework combined with Markov Chain Monte Carlo (MCMC) sampling (L. Posti et al. 2019; P. E. Mancera Piña et al. 2022b; E. M. Di Teodoro et al. 2023), using the Python implementation *emcee* (D. Foreman-Mackey et al. 2013). By employing an MCMC sampler, we explore the parameter space defined by halo mass (M_{200}) and halo concentration (c_{200}). Our goal is to constrain these key parameters by fitting theoretical rotation curves to the observed galaxy kinematics. We assume a ΛCDM cosmology and adopt standard values for the critical density ($\rho_{\rm crit}$) and gravitational constant (G). We use a standard χ^2 likelihood function $\mathcal{L}$,

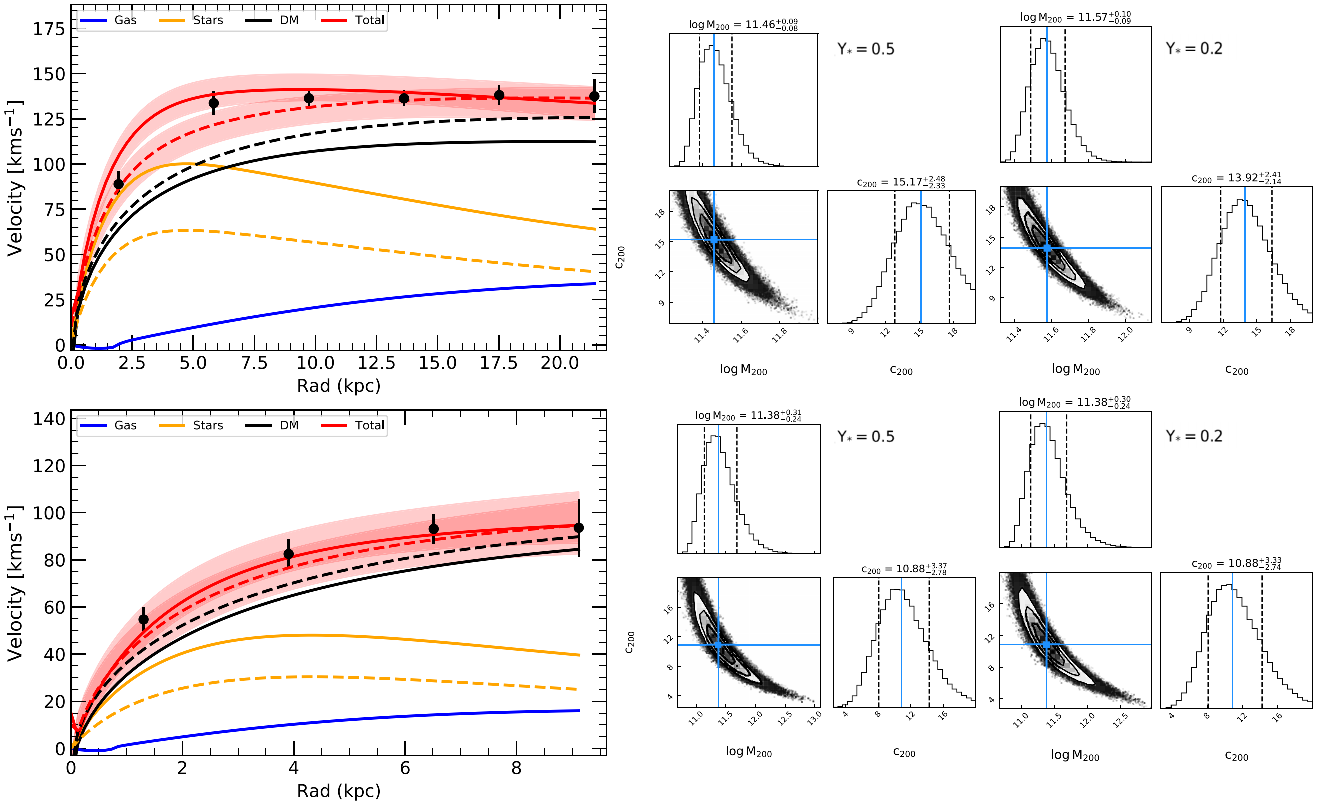

Figure 8. Mass modelling of the NFW halo profile for two galaxies J095720.6+015507 and J100211.2+020118. The upper panel shows the rotation curve decomposition for a galaxy with a poly-exponential stellar disc, and the lower panel for a galaxy with a pure exponential disc. The decomposition is shown for fixed Υ_* values, with solid lines corresponding to $\Upsilon_* = 0.5$ and dashed lines to $\Upsilon_* = 0.2$. The posteriors for these fits are shown on the right.

defined as

$$\chi^2 = -2\ln\mathcal{L}(V_{\rm rot} \mid V_{\rm mod}(x)) = \sum_{i=1}^{N}\left(\frac{V_{\rm rot}(r_i) - V_{\rm mod}(r_i)}{\Delta_i}\right)^2, \quad (11)$$

where $V_{\rm rot}(r_i)$ and $V_{\rm mod}(r_i)$ are the observed and modelled circular velocities at the ith radius r_i, respectively, and Δ_i are the uncertainties on the rotation velocity (E. M. Di Teodoro et al. 2023).

We impose physically motivated priors on the fitted parameters during the MCMC sampling. For M_{200} we use a uniform prior over a wide range $6 < \log{(M_{\rm h}/{\rm M}_{\odot})} \leq 15$. For the halo concentration instead, we use a lognormal prior based on the mass–concentration relation derived from simulations, enforcing that $\log_{10}(c_{200})$ follows a normal distribution with a mass-dependent mean and a fixed standard deviation of 0.11 dex (A. A. Dutton & A. V. Macciò 2014). This choice is motivated by the studies of H. Katz et al. (2017) and L. Posti et al. (2019), who have shown that even with high-quality local data a strong non-uniform prior on c_{200} is necessary to obtain proper constraints on the DM halo parameters (but see also P. E. Mancera Piña et al. 2022b). Indeed, in CDM cosmological simulations, the halo concentration c_{200} is not independent of M_{200}. Instead, there is a well-known mass–concentration relation, typically showing that higher-mass haloes tend to have lower concentrations. This anticorrelation arises from the formation history of haloes. Less massive haloes typically collapse earlier, when the mean background density is higher. Early collapse leads to denser central regions and thus higher concentrations. More massive haloes, on the other hand, often form later through mergers and the accretion of matter from a lower density environment. As a result, their central regions are less compact, resulting in lower concentrations. This relation encodes information about the formation epoch and assembly history of haloes, showing that their structure cannot be understood as simple scaled versions of one another (A. A. Dutton & A. V. Macciò 2014; A. D. Ludlow et al. 2014; B. Diemer & M. Joyce 2019).

For each fitting run we used 100 walkers for 5000 steps, discarding the first 20 per cent as a burn-in phase. We verify that our fits have converged by computing the integrated autocorrelation time τ and ensuring that each walker contributes at least 50τ samples. Each fitted parameter's central value was taken as the median of its posterior (50th percentile), and uncertainties were defined by the 16th and 84th percentiles. We perform three modelling runs for each galaxy, one with resolved Υ_*, and another two with Υ_* fixed at values of 0.2 and 0.5, as described in Section 5.

To assess the quality of the fit and model complexity, we use the Bayesian Information Criterion (BIC):

$$\mathrm{BIC} = -2\ln(\hat{\mathcal{L}}) + k\ln(n), \quad (12)$$

where $\hat{\mathcal{L}}$ is the maximum value of the likelihood function for the model, k is the number of free parameters, and n is the number of data points. The BIC provides a means to compare different models and assumptions about the most suitable Υ_*.

The results for two representative galaxies using $\Upsilon_* = 0.5$ and $\Upsilon_* = 0.2$ are shown in Fig. 8. The figure presents the rotation-curve decomposition, alongside the posterior distributions of the fitted parameters. The M_{200} and c_{200} parameters are tightly con-

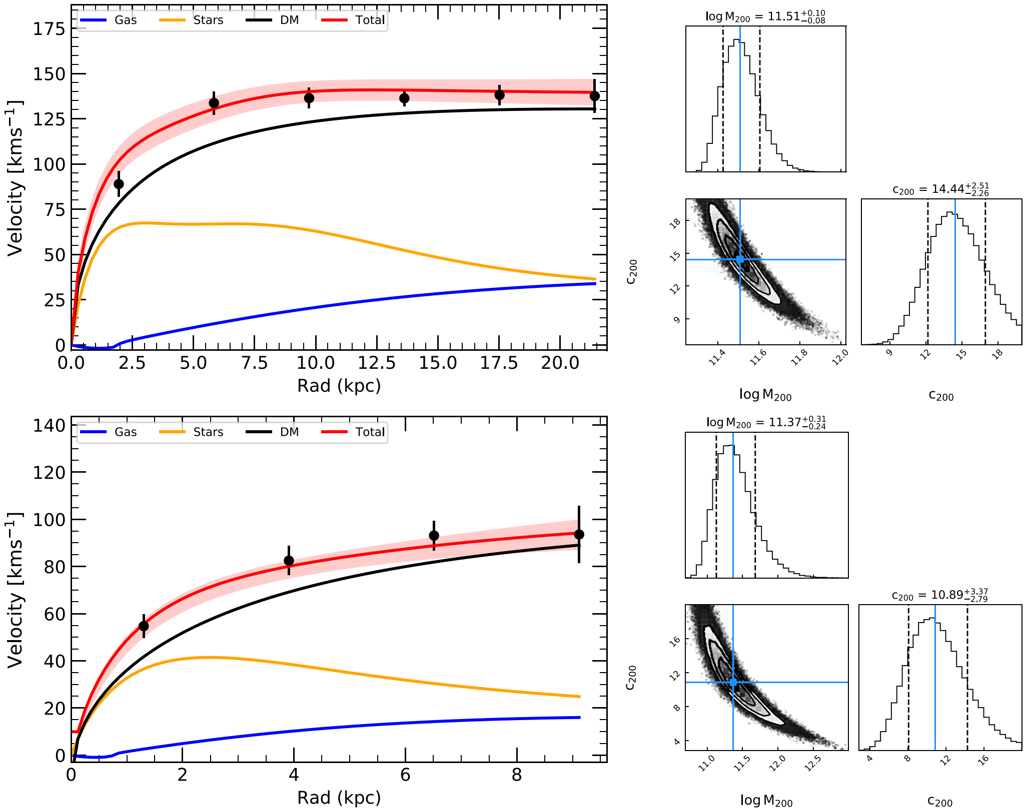

Figure 9. Mass modelling of the NFW halo profile for two galaxies J095720.6+015507 and J100211.2+020118 using the resolved stellar surface mass density. The upper panel shows the rotation curve decomposition for a galaxy with a poly-exponential stellar disc, and the lower panel for a galaxy with a pure exponential disc. The posteriors for these fits are shown on the right.

strained, with the posterior distribution of the latter reflecting the imposed mass–concentration relation. This indicates that the dark-matter halo properties are well constrained by the data, largely independently of the adopted stellar mass-to-light ratio. The BIC generally favours the models with $\Upsilon_* = 0.5$, with $\langle \mathrm{BIC}_{0.5} - \mathrm{BIC}_{0.2} \rangle = -29$ (R. E. Kass & A. E. Raftery 1995). From Fig. 8, it is clear that the main difference between the total rotation curves obtained using the two different Υ_* values is confined to the central regions of the galaxies. At larger radii, the models converge and therefore reproduce the outer rotation velocities equally well, demonstrating that uncertainties in the stellar mass prescription primarily affect the inner mass distribution, while the outer rotation curve is dominated by the halo.

Fig. 9 shows the same rotation-curve decomposition for the same galaxies, but using resolved stellar surface mass density profiles rather than the IRAC 1 surface-brightness profiles scaled by a fixed Υ_*. Overall, model comparison based on the BIC shows a strong preference for the resolved-Υ_* prescription, with mean offsets of $\langle \mathrm{BICresolved} - \mathrm{BIC0.2} \rangle = -47$ and $\langle \mathrm{BICresolved} - \mathrm{BIC0.5} \rangle = -15$. From Fig. 9 (upper panel), we can see that the model reproduces the observed rotation curve and its features more accurately when the resolved stellar mass surface density is used, with $\mathrm{BIC}_{\mathrm{resolved}} = 597$, compared to $\mathrm{BIC}_{0.5} = 658$ and $\mathrm{BIC}_{0.2} = 834$. This improvement reflects the ability of the resolved stellar mass distribution to capture radial variations in the stellar contribution, rather than simply rescaling a fixed light profile, and demonstrates that incorporating spatially resolved stellar mass information leads to a more accurate description of the observed rotation curve, although we note that the best-fitting parameters for M_{200} and c_{200} are formally consistent across all tested values of Υ_*. The M_{200} obtained using different Υ_* prescriptions are listed in Table A2.

6.1 Halo mass scaling relations

Having derived the halo masses from our rotation curve decompositions, we now examine how these haloes relate to their stellar and baryonic content. By combining our halo mass estimates with stellar masses, we first explore the SHMR. The SHMR describes how the stellar mass of galaxies is connected to the mass of their surrounding DM halo. In essence, it quantifies the efficiency with which baryonic matter is converted into stars at different halo mass scales. Lower mass haloes tend to be less efficient at forming stars (e.g. L. Posti et al. 2019; P. E. Mancera Piña et al. 2025), presumably due to a combination of factors such as supernova feedback and reionization, while intermediate-mass haloes are often thought to be most efficient, and very massive haloes may again show reduced star formation efficiency, potentially due to active galactic nuclei feedback and virial shock heating (A. Vale & J. P. Ostriker 2008; C. Conroy & R. H. Wechsler 2009; B. P. Moster et al. 2010). In theoretical work, the SHMR is usually derived via AM between stellar mass functions and DM-only simulations (P. S. Behroozi, R. H. Wechsler & C. Conroy 2013; B. P. Moster, T. Naab & S. D. M. White 2013; P. Behroozi et al. 2019), while observational analyses test whether these relations hold for real galaxies (L. Posti et al. 2019; E. M. Di Teodoro et al. 2023).

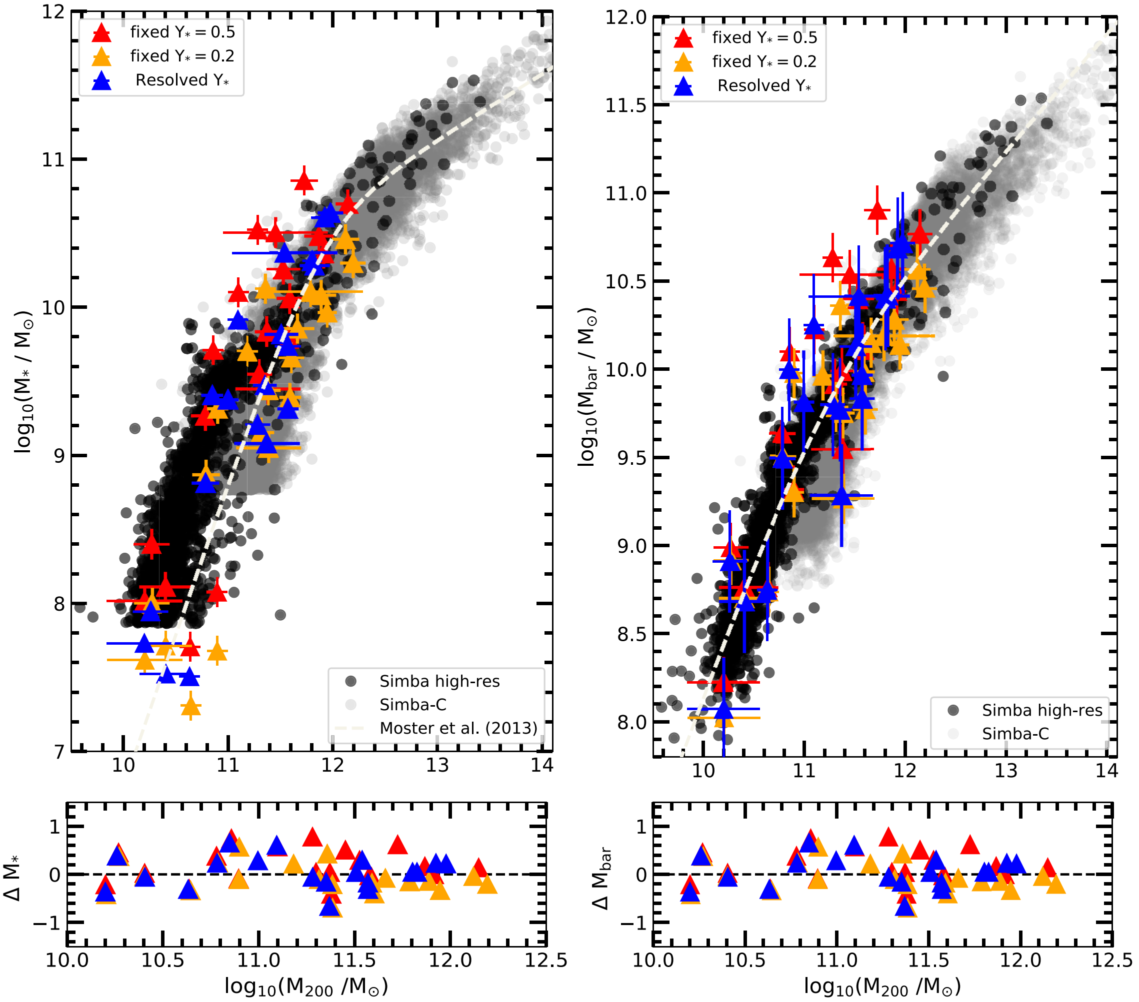

Figure 10. Left: SHMR for our sample galaxies derived under different Υ_* assumptions. The red triangles indicate results obtained with fixed $\Upsilon_* = 0.5$, orange symbols correspond to fixed $\Upsilon_* = 0.2$, and the blue symbols represent models where Υ_* is left free. Predictions from the SIMBA-C cosmological hydrodynamical simulations are shown as grey points, while the SIMBA high-resolution run is represented by black points. The abundance-matching relation from B. P. Moster et al. (2013) is shown as the dashed white line. Right: BHMR for the same sample. The dashed white line indicates the fitted relation to the theoretical models. The lower panels show the residuals with respect to the corresponding theoretical relations.

These studies highlight the importance of feedback processes and environmental effects in shaping the interplay between DM and baryons. The SHMR therefore links the growth of stellar mass in galaxies to the assembly of their DM haloes, providing critical tests for theoretical models of galaxy formation and evolution.

Fig. 10 (left) illustrates the SHMR for our sample, computed under three different assumptions for the stellar mass. We quantify the impact of different stellar-mass prescriptions on the inferred halo mass by performing object-by-object comparisons of halo masses obtained from rotation-curve decomposition for the same galaxies, and by characterizing the resulting differences through their median offsets and dispersion. Comparing the two fixed mass-to-light ratio prescriptions ($\Upsilon_* = 0.5$ and $\Upsilon_* = 0.2$) provides a direct measure of the classical disc–halo degeneracy: increasing the stellar mass through a higher global Υ_* leads to a systematic, although weak, decrease in the inferred halo mass. In our sample, a change of ~0.4 dex in stellar mass corresponds to a median decrease of ~0.05 dex in M_{200}, with this inverse trend present across the galaxy population, demonstrating that while the inner mass decomposition remains degenerate, the total halo mass is only weakly sensitive to even extreme assumptions about the global stellar mass-to-light ratio.

The behaviour changes when adopting spatially resolved stellar-mass distributions. In this case, despite a systematic reduction in stellar mass, the inferred halo masses do not show a coherent decrease relative to the fixed-Υ_* models. Instead, the median shift in M_{200} is small (~0.01 dex), more than an order of magnitude smaller than the intrinsic object-to-object scatter (~0.08 dex), indicating that the differences are dominated by galaxy-to-galaxy variation rather than a population-level offset. This demonstrates that allowing Υ_* to vary with radius does not result in a simple global trade-off between stellar and halo components, but instead introduces galaxy-specific responses that lead to a non-uniform impact on the inferred halo mass.

To assess which stellar-mass prescription is most consistent with theoretical expectations, we compare the three samples to the stellar–halo mass relation of B. P. Moster et al. (2013) by evaluating the residuals in $\log M_*$ at fixed M_{200}. The fixed $\Upsilon_* = 0.5$ sample lies systematically above the relation, with a median offset of +0.39 dex, while the fixed $\Upsilon_* = 0.2$ sample lies below it, with a median offset of −0.15 dex. In contrast, the sample based on spatially resolved stellar-mass distributions is much more closely aligned with the theoretical relation, exhibiting a median offset of only +0.08 dex. This offset is smaller in magnitude than for either fixed-Υ_* case and is comparable to the intrinsic scatter of the relation, indicating that the resolved-Υ_* prescription yields stellar–halo mass measurements that are most consistent with the canonical abundance-matching expectation. For visualization purposes, we also include data from the hydrodynamic cosmological simulations SIMBA (SIMBA-C and high resolution run; R. Davé et al. 2019), which show overall consistency with the abundance-matching relation of B. P. Moster et al. (2013) across the considered mass range (Fig. 10, left).

Incorporating H I gas mass measurements, we also construct the BHMR. BHMR extends the concept of the SHMR by considering not only the stellar mass but also the cold gas mass ($\mathrm{M}_* + 1.4\,\mathrm{M}_{\mathrm{HI}}$) to form a more complete picture of a galaxy's total baryon content relative to its host halo. While the SHMR focuses on the efficiency of converting baryons into stars, the baryonic mass-to-halo mass relation captures both the accumulation and retention of baryons, as well as their conversion into stars. By examining the baryonic content, rather than just the stellar component, we can gain insight into how efficient galaxies are at acquiring gas, how much of that gas is converted into stars, and how much is lost through outflows (E. Papastergis et al. 2012; S. S. McGaugh & J. M. Schombert 2015; P. E. Mancera Piña et al. 2025).

Fig. 10 (right) presents the BHMR for our sample under the three Υ_* assumptions, alongside the BHMR derived from the SIMBA cosmological simulations. From SIMBA we consider two runs: the 'flagship' 100 Mpc h^{-1} box run (minimum stellar mass resolution of 5.85×10^8 $\mathrm{M}_\odot$ for all galaxies considered) from the recently updated SIMBA-C simulation (R. T. Hough et al. 2023), which incorporates improved chemical enrichment models, and a high-resolution SIMBA run designed to resolve low-mass galaxies (minimum stellar mass resolution of 7.30×10^7 $\mathrm{M}_\odot$), similar to those in our sample. We limit the comparison to central galaxies, rather than including satellites to better match the MIGHTEE-H I sample.

As there is no established reference relation for the BHMR, we fit a double power-law relation to the high-resolution SIMBA sample to provide a baseline against which our observational samples can be compared (Fig. 10, right). The best-fitting double power-law parameters are $\log M_1 = 11.17 \pm 0.20$, $\log N = -1.44 \pm 0.03$ ($N = 0.0364$), $\beta = 0.60 \pm 0.08$, and $\gamma = 0.34 \pm 0.07$, where M_1 is the characteristic halo mass at which the relation transitions between the low- and high-mass regimes, N sets the overall normalization, and β and γ describe the low- and high-mass slopes, respectively. Relative to this relation the sample assuming a fixed $\Upsilon_* = 0.5$ lies systematically above the fitted relation, with a median offset of ∼0.09 dex, while the fixed $\Upsilon_* = 0.2$ sample lies below it, with a median offset of ∼−0.12 dex. In contrast, the sample based on spatially resolved stellar-mass estimates shows the closest agreement, exhibiting a median offset of only ∼0.04 dex. This behaviour is qualitatively similar to that found for the SHMR AM model, where different stellar-mass assumptions systematically shift galaxies above or below the mean relation, while prescriptions that more accurately capture the stellar mass distribution yield the closest correspondence to the theoretical predictions. It is important to note that several studies have reported deviations from the AM predictions, particularly at high mass scales (L. Posti et al. 2019; E. M. Di Teodoro et al. 2023), but see H. Desmond & R. H. Wechsler (2015) and F. Boreiko et al. (2026) for analyses of how sample selection may impact this. We do not observe such departures within the mass range probed by our sample. This further motivates the use of spatially resolved SED-based mass-to-light ratios in upcoming larger samples. The resulting median offsets and scatter of each sample relative to the theoretical relations are listed in Table 1.

Table 1. Table summarizing the median offsets (Δ) from the theoretical SHMR and BHMR relations for our sample under different Υ_* assumptions (Fig. 10), along with the observed scatter (σ) relative to the theoretical relations. All values are expressed in dex.

	Med Δ		σ	
	$M_\star$	M_{bar}	$M_\star$	M_{bar}
$\Upsilon_* = 0.5$	+0.39	+0.09	0.51	0.33
$\Upsilon_* = 0.2$	−0.15	−0.12	0.48	0.30
Resolved Υ_*	+0.08	0.04	0.43	0.29

7 SUMMARY AND CONCLUSIONS

In this paper, we use deep H I observations from the MIGHTEE survey to derive high-quality H I rotation curves for a sample of 20 galaxies in the COSMOS field across a previously unexplored redshift range, $0 \leq z \leq 0.08$. Combining H I rotation curves with carefully derived stellar surface brightness profiles from *Spitzer* IRAC 1 (3.6 μm) band data and resolved stellar mass surface densities profiles from A. A. Vărăşteanu et al. (**2025**), we explore mass models for our sample galaxies using the rotation curve decomposition technique. We derived DM halo masses by fitting the observed rotation curves with a parametric NFW halo model (J. F. Navarro et al. 1996), combined with our baryonic mass profiles. Using a Bayesian MCMC approach, we explored the parameter space to find the best-fitting halo mass and concentration. By decomposing the H I rotation curves into their baryonic and DM components, we obtain observational constraints on the DM halo masses of our sample galaxies and investigate how the DM haloes connect to their stellar and baryonic content.

Our main results can be summarized as follows:

(i) Examining the ratio of the baryonic velocity contribution (V_{bar}) to the total observed velocity (V_{obs}) at the characteristic radius $R_{2.2}$, we find that adopting a higher stellar mass-to-light ratio ($\Upsilon_* = 0.5$) produces a clear dependence of $V_{2.2}/V_{\mathrm{obs}}$ on total galaxy luminosity, consistent with previous studies of nearby disc galaxies (F. Lelli et al. 2016). In this case, more luminous systems approach $V_{\mathrm{bar}} \approx V_{\mathrm{obs}}$ at $R_{2.2}$, indicating an increased relative baryonic contribution in the inner regions. In contrast, this luminosity dependence largely disappears when a lower value of $\Upsilon_* = 0.2$ is assumed, resulting in an almost flat $V_{2.2}/V_{\mathrm{obs}}$–luminosity relation (Fig. 7). This demonstrates that the inferred dynamical role of baryons is highly sensitive to the assumed stellar mass-to-light ratio.

Crucially, when resolved stellar mass surface density profiles are used instead of a fixed Υ_*, the physically meaningful dependence of $V_{2.2}/V_{\mathrm{obs}}$ on luminosity is preserved, with a slope comparable to that obtained for $\Upsilon_* = 0.5$, while avoiding the suppression of this trend seen for $\Upsilon_* = 0.2$. This shows that allowing for galaxy-dependent and radially varying stellar mass-to-light ratios provides a more realistic description of the stellar contribution to galaxy dynamics. These results highlight that the disc–halo degeneracy is strongly amplified by the assumption of a universal stellar mass-to-light ratio, and that incorporating resolved stellar mass information offers a more physically motivated framework for interpreting rotation curves in the context of galaxy formation models and the interplay between baryonic and DM.

(ii) Comparing rotation-curve decompositions based on fixed and resolved stellar mass prescriptions, we find that differences between models with fixed Υ_* are confined to the central regions, while the outer rotation curves are reproduced equally well, indicating that uncertainties in the stellar mass primarily affect the inner mass distribution (Fig. 8). Using resolved stellar surface mass density profiles yields a statistically preferred description of the data, improving the reproduction of detailed rotation-curve features (Fig. 9). This demonstrates that incorporating spatially resolved stellar mass information provides a more accurate and physically motivated representation of galaxy rotation curves than globally scaled light profiles.

(iii) By comparing stellar–halo mass relations derived under different stellar-mass prescriptions, we show that the inferred total halo mass is only weakly sensitive to even extreme assumptions about a global stellar mass-to-light ratio. While fixed-Υ_* models exhibit the expected inverse response between stellar and halo mass, the resulting shifts in M_{200} are small compared to the intrinsic galaxy-to-galaxy scatter. Adopting spatially resolved stellar-mass distributions further alters this behaviour: variations in stellar mass do not translate into a coherent population-level shift in halo mass, but instead produce galaxy-specific responses in the mass decomposition (Fig. 10 left). When compared to the theoretical abundance-matching expectations (B. P. Moster et al. 2010), the resolved-stellar-mass case yields the smallest residuals and the closest overall agreement, indicating that allowing for radial variations in the stellar mass provides a more internally consistent mapping between stellar and halo mass than either fixed-Υ_* assumption.

(iv) By incorporating H I gas mass measurements, we extend our analysis to the BHMR, which provides a more complete view of the total baryon content of galaxies relative to their host haloes. Comparing our observational BHMR to SIMBA simulations, we find that different stellar mass-to-light ratio assumptions systematically shift galaxies relative to the simulation-based reference relation: fixed $\Upsilon_* = 0.5$ places galaxies above the relation, while $\Upsilon_* = 0.2$ shifts them below it. In contrast, stellar masses derived from spatially resolved measurements yield the smallest offsets and the closest overall agreement with the fitted SIMBA baseline (Fig. 10 right). This behaviour mirrors that observed for the SHMR, indicating that prescriptions that more accurately capture the stellar mass distribution also provide the most consistent mapping between baryonic mass and halo mass, and minimize systematic biases when comparing observations to theoretical predictions.

In conclusion, studies of galaxy rotation curves and mass modelling provide key insights into the nature of DM, the distribution of baryonic matter, and the physical processes governing galaxy formation and evolution. With current and forthcoming observational facilities, such as the SKA, extending these analyses to higher redshifts will enable us to trace the evolution of mass distributions over cosmic time, offering stringent tests of cosmological models.

In this paper, we have demonstrated that employing spatially resolved SED fitting across a broad wavelength range provides a powerful avenue for mitigating the disc–halo degeneracy. By mapping stellar populations and dust content across galaxies, resolved SED modelling yields spatially resolved stellar mass surface density profiles, removing the need to assume a single global mass-to-light ratio. This multiwavelength approach, spanning ultraviolet to infrared bands, naturally accounts for variations in stellar population age, metallicity, and dust attenuation, all of which have a strong impact on inferred mass-to-light ratios. Incorporating this information into mass modelling leads to a more physically motivated characterization of the stellar mass distribution and enables a clearer separation between baryonic and dark-matter contributions to galaxy rotation curves.

At the same time, important observational challenges remain. The limited spatial resolution of current H I data beyond the very local universe (A. A. Ponomareva et al. 2021), together with the signal-to-noise limitations of large H I surveys (N. Deg et al. 2024), restrict our ability to probe the gravitational potential in the innermost regions of galaxies. As a result, distinguishing robustly between different dark-matter halo models, such as cored versus cuspy profiles, remains difficult (W. J. G. Blok & S. S. McGaugh 1997; S. Kurapati et al. 2020; P. E. Mancera Piña et al. 2025). Future progress will therefore rely on multiwavelength synergies, particularly the combination of H I data with high-resolution optical emission-line observations (e.g. Hα) that trace the inner galaxy regions (E. M. Di Teodoro et al. 2023). Such joint analyses will improve constraints on the central mass distribution, further reduce modelling degeneracies, and provide stronger tests of dark-matter halo structure.

ACKNOWLEDGEMENTS

We thank the anonymous referee for helpful comments that significantly improved this paper.

AAP is grateful to Giuliano Iorio for making GALPYNAMICS publicly available and for providing support in its use.

The MeerKAT telescope is operated by the South African Radio Astronomy Observatory, which is a facility of the National Research Foundation, an agency of the Department of Science and Innovation. We acknowledge use of the Inter-University Institute for Data Intensive Astronomy (IDIA) data intensive research cloud for data processing. IDIA is a South African university partnership involving the University of Cape Town, the University of Pretoria and the University of the Western Cape. The authors acknowledge the Centre for High Performance Computing (CHPC), South Africa, for providing computational resources to this research project.

This work is based in part on archival data obtained with the *Spitzer Space Telescope*, which was operated by the Jet Propulsion Laboratory, California Institute of Technology under a contract with NASA. Support for this work was provided by an award issued by JPL/Caltech.

This work is based in part on data products produced at Terapix available at the Canadian Astronomy Data Centre as part of the Canada–France–Hawaii Telescope Legacy Survey, a collaborative project of NRC and CNRS. The Hyper SuprimeCam (HSC) collaboration includes the astronomical communities of Japan and Taiwan, and Princeton University. The HSC instrumentation and software were developed by the National Astronomical Observatory of Japan (NAOJ), the Kavli Institute for the Physics and Mathematics of the Universe (Kavli IPMU), the University of Tokyo, the High Energy Accelerator Research Organization (KEK), the Academia Sinica Institute for Astronomy and Astrophysics in Taiwan (ASIAA), and Princeton University. Funding was contributed by the FIRST program from Japanese Cabinet Office, the Ministry of Education, Culture, Sports, Science and Technology (MEXT), the Japan Society for the Promotion of Science (JSPS), Japan Science and Technology Agency (JST), the Toray Science Foundation, NAOJ, Kavli IPMU, KEK, ASIAA, and Princeton University.

AAP, MJJ, and IH acknowledge support of the STFC consolidated grant ST/S000488/1. MJJ, IH, AV, TY, HP, and SK acknowledge the support of a UKRI Frontiers Research Grant [EP/X026639/1], which was selected by the European Research Council. MJJ and AAP acknowledge support from the Oxford Hintze Centre for Astrophysical Surveys, which is funded through generous support from the Hintze Family Charitable Foundation. PEMP acknowledges the support from the Dutch Research Council (NWO) through the Veni grant VI.Veni.222.364. IH acknowledges support from the South African Radio Astronomy Observatory (SARAO), which is a facility of the National Research Foundation (NRF), an agency of the Department of Science and Innovation. MG is supported by the UK STFC Grant ST/Y001117/1. MG acknowledges support from the Inter-University Institute for Data Intensive Astronomy (IDIA). HD is supported by a Royal Society University Research Fellowship (grant no. 211046). KAO acknowledges support by the Royal Society through a Dorothy Hodgkin Fellowship (DHF/R1/231105). IP acknowledges support from the Italian Ministry of Foreign Affairs and International Cooperation (grant number PGR ZA23GR03) and from INAF under the Large Grant 2022 funding scheme (project ‘MeerKAT and LOFAR Team up: a Unique Radio Window on Galaxy/AGN co-Evolution’). MB and AG gratefully acknowledge the financial support from the Flemish Fund for Scientific Research (FWO-Vlaanderen) and the South African National Research Foundation (NRF) under their Bilateral Scientific Cooperation program (grant G0G0420N). They also acknowledge the support of networking activities by NRF and the Belgian Science Policy Office (BELSPO), under grant BL/02/SA12 (GALSIMAS).

For the purpose of open access, the author has applied a Creative Commons Attribution (CC BY) licence to any Author Accepted Manuscript version arising from this submission.

This research has made use of NASA’s Astrophysics Data System Bibliographic Services. This research made use of Astropy,[3] a community-developed core Python package for Astronomy.

DATA AVAILABILITY

The raw visibility data are publicly available from the SARAO archive by searching for the capture block IDs listed in Table 1 of I. Heywood et al. (2024). The Spitzer IRAC 1 images used in this work are also publicly accessible as part of S-COSMOS (D. B. Sanders et al. 2007). Tables summarizing the main properties of the sample and the derived parameters are provided in the appendix (Tables A1 and A2). All data involved in the analysis are available upon reasonable request to the corresponding author.

REFERENCES

Aihara H. et al., 2018, PASJ, 70, S4
Aihara H. et al., 2019, PASJ, 71, 114
Allaert F., Gentile G., Baes M., 2017, A&A, 605, A55
Aniyan S. et al., 2018, MNRAS, 476, 1909
Aniyan S., Ponomareva A. A., Freeman K. C., Arnaboldi M., Gerhard O. E., Coccato L., Kuijken K., Merrifield M., 2021, MNRAS, 500, 3579
Arnett D., 1999, Ap&SS, 265, 29
Bacchini C., Fraternali F., Iorio G., Pezzulli G., 2019, A&A, 622, A64
Balmaverde B. et al., 2021, A&A, 645, A12
Begeman K. G., 1989, A&A, 223, 47
Begeman K. G., Broeils A. H., Sanders R. H., 1991, MNRAS, 249, 523
Behroozi P., Wechsler R. H., Hearin A. P., Conroy C., 2019, MNRAS, 488, 3143
Behroozi P. S., Wechsler R. H., Conroy C., 2013, ApJ, 770, 57
Bershady M. A., Verheijen M. A. W., Swaters R. A., Andersen D. R., Westfall K. B., Martinsson T., 2010, ApJ, 716, 198
Binney J., Tremaine S., 2008, Galactic Dynamics: Second Edition. Princeton University Press, Princeton, NJ
Boreiko F., Yasin T., Desmond H., Stiskalek R., Jarvis M. J., 2026, preprint (arXiv:2601.07799)
Bosma A., 1978, PhD thesis, Univ. Groningen, Netherlands
Bosma A., 1981, AJ, 86, 1825
Ciotti L., Bertin G., 1999, A&A, 352, 447
Combes F. et al., 2019, A&A, 623, A79
Comerón S., Salo H., Knapen J. H., 2018, A&A, 610, A5
Conroy C., Wechsler R. H., 2009, ApJ, 696, 620
Davé R., Anglés-Alcázar D., Narayanan D., Li Q., Rafieferantsoa M. H., Appleby S., 2019, MNRAS, 486, 2827
de Blok W. J. G., McGaugh S. S., 1997, MNRAS, 290, 533
de Blok W. J. G., Walter F., Brinks E., Trachternach C., Oh S. H., Kennicutt R. C. J., 2008, AJ, 136, 2648
de Blok W. J. G., 2010, Adv. Astron., 2010, 789293
de Blok W. J. G. et al., 2016, AJ, 152, 51
Deg N. et al., 2022, Publ. Astron. Soc. Aust., 39, e059
Deg N. et al., 2024, ApJ, 976, 159
Desmond H., Wechsler R. H., 2015, MNRAS, 454, 322
Di Cintio A., Lelli F., 2016, MNRAS, 456, L127
Di Cintio A., Brook C. B., Dutton A. A., Macciò A. V., Stinson G. S., Knebe A., 2014, MNRAS, 441, 2986
Di Teodoro E. M., Fraternali F., 2015, MNRAS, 451, 3021
Di Teodoro E. M. et al., 2023, MNRAS, 518, 6340
Diemer B., Joyce M., 2019, ApJ, 871, 168
Dutton A. A., Macciò A. V., 2014, MNRAS, 441, 3359
Foreman-Mackey D., Hogg D. W., Lang D., Goodman J., 2013, PASP, 125, 306
Fouque P., Bottinelli L., Gouguenheim L., Paturel G., 1990, ApJ, 349, 1
Frank B. S., de Blok W. J. G., Walter F., Leroy A., Carignan C., 2016, AJ, 151, 94
Freeman K. C., 1970, ApJ, 160, 811
Heald G. et al., 2011, A&A, 526, A118
Heywood I. et al., 2024, MNRAS, 534, 76
Hough R. T., Rennehan D., Kobayashi C., Loubser S. I., Davé R., Babul A., Cui W., 2023, MNRAS, 525, 1061
Howell S. B., 2006, Cambridge Observing Bandbooks for Research Astronomers, Vol. 5, Handbook of CCD Astronomy. Cambridge Univ. Press, Cambridge, UK
Ianjamasimanana R., de Blok W. J. G., Walter F., Heald G. H., Caldú-Primo A., Jarrett T. H., 2015, AJ, 150, 47
Iorio G., Fraternali F., Nipoti C., Di Teodoro E., Read J. I., Battaglia G., 2017, MNRAS, 466, 4159
Jarvis M. et al., 2016, preprint (arXiv:1709.01901)
Jarvis M. J. et al., 2013, MNRAS, 428, 1281
Jonas J. L., 2009, IEEE Proc., 97, 1522
Kamphuis P., Józsa G. I. G., Oh S.. H., Spekkens K., Urbancic N., Serra P., Koribalski B. S., Dettmar R. J., 2015, MNRAS, 452, 3139
Kass R. E., Raftery A. E., 1995, J. Am. Stat. Assoc., 90, 773
Katz H., Lelli F., McGaugh S. S., Di Cintio A., Brook C. B., Schombert J. M., 2017, MNRAS, 466, 1648
Klypin A. A., Trujillo-Gomez S., Primack J., 2011, ApJ, 740, 102
Kormendy J., Kennicutt Robert C. J., 2004, ARA&A, 42, 603
Kurapati S., Chengalur J. N., Kamphuis P., Pustilnik S., 2020, MNRAS, 491, 4993

---

[3] http://www.astropy.org

Lelli F., McGaugh S. S., Schombert J. M., 2016, AJ, 152, 157
Ludlow A. D., Navarro J. F., Angulo R. E., Boylan-Kolchin M., Springel V., Frenk C., White S. D. M., 2014, MNRAS, 441, 378
Maddox N. et al., 2021, A&A, 646, A35
Mancera Piña P. E. et al., 2020, MNRAS, 495, 3636
Mancera Piña P. E., Posti L., Fraternali F., Adams E. A. K., Oosterloo T., 2021, A&A, 647, A76
Mancera Piña P. E., Fraternali F., Oosterloo T., Adams E. A. K., Oman K. A., Leisman L., 2022a, MNRAS, 512, 3230
Mancera Piña P. E., Fraternali F., Oosterloo T., Adams E. A. K., di Teodoro E., Bacchini C., Iorio G., 2022b, MNRAS, 514, 3329
Mancera Piña P. E., Golini G., Trujillo I., Montes M., 2024, A&A, 689, A344
Mancera Piña P. E., Read J. I., Kim S., Marasco A., Benavides J. A., Glowacki M., Pezzulli G., Lagos C. d. P., 2025, A&A, 699, A311
Mancera Piña P. E., Di Teodoro E. M., Fall S. M., Marasco A., Kriek M., Martorano M., 2026, A&A, 705, A180
Marasco A., Posti L., Oman K., Famaey B., Cresci G., Fraternali F., 2020, A&A, 640, A70
Marasco A. et al., 2023, A&A, 670, A92
Marasco A., Fall S. M., Di Teodoro E. M., Mancera Piña P. E., 2025, A&A, 695, L23
Martinsson T. P. K., Verheijen M. A. W., Westfall K. B., Bershady M. A., Andersen D. R., Swaters R. A., 2013, A&A, 557, A131
Martinsson T. P. K., Verheijen M. A. W., Bershady M. A., Westfall K. B., Andersen D. R., Swaters R. A., 2016, A&A, 585, A99
McCracken H. J. et al., 2012, A&A, 544, A156
McGaugh S. S., Schombert J. M., 2014, AJ, 148, 77
McGaugh S. S., Schombert J. M., 2015, ApJ, 802, 18
McGaugh S. S., Schombert J. M., Bothun G. D., de Blok W. J. G., 2000, ApJ, 533, L99
McGaugh S. S., Lelli F., Schombert J. M., 2016, Phys. Rev. Lett., 117, 201101
Meidt S. E. et al., 2012, ApJ, 744, 17
Meidt S. E. et al., 2014, ApJ, 788, 144
Meyer M., Robotham A., Obreschkow D., Westmeier T., Duffy A. R., Staveley-Smith L., 2017, Publ. Astron. Soc. Aust., 34, e052
Mogotsi K. M., de Blok W. J. G., Caldú-Primo A., Walter F., Ianjamasimanana R., Leroy A. K., 2016, AJ, 151, 15
Moster B. P., Somerville R. S., Maulbetsch C., van den Bosch F. C., Macciò A. V., Naab T., Oser L., 2010, ApJ, 710, 903
Moster B. P., Naab T., White S. D. M., 2013, MNRAS, 428, 3121
Navarro J. F., Frenk C. S., White S. D. M., 1996, ApJ, 462, 563
Oh S.-H. et al., 2015, AJ, 149, 180
Papastergis E., Cattaneo A., Huang S., Giovanelli R., Haynes M. P., 2012, ApJ, 759, 138
Planck Collaboration VI, 2020, A&A, 641, A6
Ponomareva A. A., Verheijen M. A. W., Bosma A., 2016, MNRAS, 463, 4052
Ponomareva A. A., Verheijen M. A. W., Peletier R. F., Bosma A., 2017, MNRAS, 469, 2387
Ponomareva A. A., Verheijen M. A. W., Papastergis E., Bosma A., Peletier R. F., 2018, MNRAS, 474, 4366
Ponomareva A. A. et al., 2021, MNRAS, 508, 1195
Ponomareva A. A. et al., 2023, MNRAS, 522, 5308
Posti L., Marasco A., Fraternali F., Famaey B., 2019, A&A, 629, A59
Querejeta M. et al., 2015, ApJS, 219, 5
Rajohnson S. H. A. et al., 2022, MNRAS, 512, 2697
Ranchod S. et al., 2021, MNRAS, 506, 2753
Read J. I., Iorio G., Agertz O., Fraternali F., 2016, MNRAS, 462, 3628
Röck B., Vazdekis A., Peletier R. F., Knapen J. H., Falcón-Barroso J., 2015, MNRAS, 449, 2853
Romeo A. B., 1992, MNRAS, 256, 307
Rubin V. C., Ford W. K. J., Thonnard N., 1978, ApJ, 225, L107
Said K., Colless M., Magoulas C., Lucey J. R., Hudson M. J., 2020, MNRAS, 497, 1275
Sanders D. B. et al., 2007, ApJS, 172, 86
Schombert J., McGaugh S., Lelli F., 2019, MNRAS, 483, 1496
Schombert J., McGaugh S., Lelli F., 2022, AJ, 163, 154
Sheth K. et al., 2010, PASP, 122, 1397
Šiljeg B. et al., 2024, A&A, 692, A217
Springel V. et al., 2005, Nature, 435, 629
Starkman N., Lelli F., McGaugh S., Schombert J., 2018, MNRAS, 480, 2292
Swaters R. A., 1999, PhD thesis, Univ. Groningen, Netherlands
Tamm A., Tempel E., Tenjes P., Tihhonova O., Tuvikene T., 2012, A&A, 546, A4
Tollet E. et al., 2016, MNRAS, 456, 3542
Tonry J. L., Blakeslee J. P., Ajhar E. A., Dressler A., 2000, ApJ, 530, 625
Tudorache M. N. et al., 2022, MNRAS, 513, 2168
Tully R. B., Fouque P., 1985, in Richter O. G., Binggeli B., eds, European Southern Observatory Conference and Workshop Proceedings Vol. 20, The Virgo Cluster Distance Corrections to Global Parameters. p. 417
Tully R. B., Courtois H. M., Sorce J. G., 2016, AJ, 152, 50
Vale A., Ostriker J. P., 2008, MNRAS, 383, 355
van Albada T. S., Sancisi R., 1986, Philos. Trans. R. Soc. A, 320, 447
van Albada T. S., Bahcall J. N., Begeman K., Sancisi R., 1985, ApJ, 295, 305
van der Kruit P. C., Freeman K. C., 2011, ARA&A, 49, 301
Vărăşteanu A. A. et al., 2025, MNRAS, 541, 2366
Venturi G. et al., 2021, A&A, 648, A17
Verheijen M. A. W., 2001, ApJ, 563, 694
Wang J., Koribalski B. S., Serra P., van der Hulst T., Roychowdhury S., Kamphuis P., Chengalur J. N., 2016, MNRAS, 460, 2143
Yoachim P., Dalcanton J. J., 2006, AJ, 131, 226

APPENDIX A: SAMPLE DATA TABLES

Tables summarizing the main properties of our sample A1 and the results of the mass modelling A2

Table A1. Table summarizing our sample main properties. Column (1): Galaxy identifier; Column (2): right ascension of the galaxy in degrees (J2000); Column (3): declination of the galaxy in degrees (J2000); Column (4): redshift derived from the H I line; Column (5): $\log_{10}$ of the galaxy's H I mass; Column (6): inclination angle (in degrees), measured from IRAC 1 imaging; Column (7): stellar disc scale length in kiloparsecs; Column (8): position angle (in deg), used for kinematic modelling; Column (9): number of the resolution elements across the major axis of the H I moment 1 map; Column (10): $\log_{10}$ of total luminosity in the Spitzer 3.6 μm band; Column (11): $\log_{10}$ of the galaxy's stellar mass derived using resolved Υ_*.

Name	RA deg	Dec. deg	z	$\log_{10}$(MHI) $M_\odot$	i° deg	h_d kpc	pa deg	Nb	$\log_{10}(L_{IR1})$ $L_\odot$	$\log_{10}(M_\star)$ $M_\odot$
J095829.1+014139	149.621	1.694	0.006	9.144 ± 0.008	66.759	1.933 ± 0.251	60.752	11	8.378 ± 0.137	–
J095846.8+022051	149.695	2.348	0.006	8.575 ± 0.015	69.235	1.034 ± 0.134	311.745	7	8.008 ± 0.133	7.485 ± 0.088
J095927.9+020025	149.866	2.007	0.013	8.505 ± 0.065	40.824	0.972 ± 0.126	293.299	3	8.412 ± 0.137	7.653 ± 0.101
J100005.8+015440	150.024	1.911	0.006	7.661 ± 0.126	65.857	0.794 ± 0.103	116.527	3	8.316 ± 0.136	7.823 ± 0.063
J095904.3+021516	149.768	2.254	0.025	8.713 ± 0.115	52.729	1.908 ± 0.248	29.397	3	8.700 ± 0.130	7.985 ± 0.085
J100211.2+020118	150.547	2.022	0.021	8.713 ± 0.119	38.652	1.936 ± 0.174	42.384	3	9.749 ± 0.087	9.181 ± 0.098
J100009.3+024247	150.039	2.713	0.033	9.472 ± 0.068	59.051	3.277 ± 0.295	336.929	5	10.402 ± 0.094	9.493 ± 0.094
J100115.2+021823	150.313	2.306	0.028	9.248 ± 0.057	72.663	3.100 ± 0.279	172.713	4	9.567 ± 0.086	8.792 ± 0.092
J095720.6+015507	149.336	1.919	0.032	9.690 ± 0.034	45.168	4.270 ± 0.384	56.609	5	10.557 ± 0.096	10.101 ± 0.076
J100143.2+024109	150.430	2.686	0.047	9.712 ± 0.065	43.408	3.513 ± 0.316	82.713	4	10.088 ± 0.091	9.433 ± 0.099
J100259.0+022035	150.746	2.343	0.044	9.769 ± 0.065	47.931	4.705 ± 0.423	256.795	6	11.156 ± 0.102	10.921 ± 0.101
J100055.2+022344	150.230	2.395	0.044	9.274 ± 0.148	44.149	2.441 ± 0.220	210.507	5	10.804 ± 0.098	10.531 ± 0.083
J095923.2+024137	149.847	2.694	0.048	8.983 ± 0.272	48.236	3.276 ± 0.295	83.175	3	10.359 ± 0.094	9.753 ± 0.105
J100236.5+014836	150.652	1.810	0.046	9.725 ± 0.043	56.564	5.582 ± 0.502	329.657	4	10.010 ± 0.090	9.474 ± 0.127
J100117.1+020337	150.321	2.060	0.062	9.317 ± 0.114	49.847	3.443 ± 0.310	138.907	3	10.138 ± 0.091	9.505 ± 0.099
J100003.9+015253	150.016	1.881	0.065	9.524 ± 0.202	60.666	3.562 ± 0.321	18.422	5	9.852 ± 0.089	9.194 ± 0.091
J095755.9+022608	149.483	2.436	0.071	9.508 ± 0.197	78.558	6.341 ± 0.571	59.042	5	10.664 ± 0.097	10.081 ± 0.104
J100217.9+015124	150.574	1.857	0.062	9.701 ± 0.088	51.440	3.743 ± 0.337	340.661	3	10.779 ± 0.098	10.312 ± 0.122
J100103.7+023053	150.265	2.515	0.072	9.837 ± 0.106	58.864	6.061 ± 0.545	83.189	5	10.824 ± 0.098	10.093 ± 0.105
J095907.8+024213	149.782	2.704	0.079	9.804 ± 0.098	49.830	8.351 ± 0.752	295.425	4	10.996 ± 0.100	10.814 ± 0.077

Table A2. Table summarizing the DM halo mass (M_{200}) obtained using different assumption of the mass-to-light ratio in mass modelling. Column (1): Galaxy identifier; Column (2): M_{200} assuming $\Upsilon_* = 0.5$; Column (3): M_{200} assuming $\Upsilon_* = 0.2$; Column (4): M_{200} assuming resolved Υ_*.

Name	$\log_{10}(M_{200}^{\Upsilon_*=0.5})$ $M_\odot$	$\log_{10}(M200_{200}^{\Upsilon_*=0.2})$ $M_\odot$	$\log_{10}(M_{200}^{SED \Upsilon_*})$ $M_\odot$
J095829.1+014139	$10.895^{+0.10}_{-0.09}$	$10.896^{+0.10}_{-0.09}$	–
J095846.8+022051	$10.638^{+0.10}_{-0.09}$	$10.645^{+0.10}_{-0.09}$	$10.632^{+0.10}_{-0.09}$
J095927.9+020025	$10.405^{+0.24}_{-0.18}$	$10.404^{+0.24}_{-0.18}$	$10.406^{+0.24}_{-0.18}$
J100005.8+015440	$10.201^{+0.35}_{-0.22}$	$10.204^{+0.34}_{-0.23}$	$10.200^{+0.35}_{-0.22}$
J095904.3+021516	$10.269^{+0.17}_{-0.14}$	$10.273^{+0.17}_{-0.14}$	$10.260^{+0.17}_{-0.14}$
J100211.2+020118	$11.431^{+0.08}_{-0.07}$	$11.553^{+0.09}_{-0.08}$	$11.369^{+0.31}_{-0.24}$
J100009.3+024247	$11.098^{+0.08}_{-0.06}$	$11.182^{+0.08}_{-0.07}$	$10.996^{+0.07}_{-0.05}$
J100115.2+021823	$10.780^{+0.13}_{-0.11}$	$10.788^{+0.13}_{-0.11}$	$10.783^{+0.13}_{-0.11}$
J095720.6+015507	$11.166^{+0.20}_{-0.15}$	$11.171^{+0.19}_{-0.15}$	$11.509^{+0.10}_{-0.08}$
J100143.2+024109	$11.578^{+0.10}_{-0.08}$	$11.591^{+0.09}_{-0.08}$	$11.570^{+0.09}_{-0.08}$
J100259.0+022035	$11.725^{+0.12}_{-0.12}$	$12.121^{+0.11}_{-0.09}$	$11.925^{+0.09}_{-0.01}$
J100055.2+022344	$11.453^{+0.29}_{-0.31}$	$11.788^{+0.28}_{-0.25}$	$11.540^{+0.18}_{-0.15}$
J095923.2+024137	$11.588^{+0.11}_{-0.09}$	$11.604^{+0.12}_{-0.10}$	$11.571^{+0.11}_{-0.09}$
J100236.5+014836	$10.858^{+0.09}_{-0.08}$	$10.899^{+0.09}_{-0.08}$	$10.848^{+0.09}_{-0.08}$
J100117.1+020337	$11.371^{+0.12}_{-0.10}$	$11.385^{+0.12}_{-0.10}$	$11.352^{+0.12}_{-0.10}$
J100003.9+015253	$11.299^{+0.08}_{-0.08}$	$11.315^{+0.08}_{-0.08}$	$11.282^{+0.08}_{-0.07}$
J095755.9+022608	$11.914^{+0.09}_{-0.08}$	$11.947^{+0.09}_{-0.08}$	$11.803^{+0.08}_{-0.07}$
J100217.9+015124	$11.867^{+0.14}_{-0.11}$	$11.888^{+0.14}_{-0.12}$	$11.826^{+0.13}_{-0.11}$
J100103.7+023053	$11.281^{+0.10}_{-0.09}$	$11.358^{+0.10}_{-0.09}$	$11.094^{+0.10}_{-0.09}$
J095907.8+024213	$12.148^{+0.12}_{-0.10}$	$12.193^{+0.12}_{-0.11}$	$11.978^{+0.11}_{-0.10}$

[1]*Centre for Astrophysics Research, School of Physics, Astronomy and Mathematics, University of Hertfordshire, College Lane, Hatfield AL10 9AB, UK*
[2]*Oxford Astrophysics, Denys Wilkinson Building, University of Oxford, Keble Road, Oxford OX1 3RH, UK*
[3]*Leiden Observatory, Leiden University, P.O. Box 9513, NL-2300 RA Leiden, the Netherlands*
[4]*Institute for Astronomy, University of Edinburgh, Royal Observatory, Edinburgh EH9 3HJ, UK*
[5]*Department of Astronomy, Inter-University Institute for Data Intensive Astronomy, University of Cape Town, Cape Town, South Africa*
[6]*Institute of Cosmology and Gravitation, University of Portsmouth, Dennis Sciama Building, Portsmouth PO1 3FX, UK*
[7]*Department of Physics and Astronomy, University of the Western Cape, Robert Sobukwe Road, Bellville 7535, South Africa*
[8]*Department of Physics and Electronics, Centre for Radio Astronomy Techniques and Technologies, Rhodes University, PO Box 94, Makhanda 6140, South Africa*
[9]*South African Radio Astronomy Observatory, 2 Fir Street, Black River Park, Observatory, Cape Town 7925, South Africa*
[10]*School of Physics, H.H. Wills Physics Laboratory, Tyndall Avenue, University of Bristol, Bristol BS8 1TL, UK*
[11]*ASTRON, the Netherlands Institute for Radio Astronomy, Oude Hoogeveesedijk 4, NL-7991 PD Dwingeloo, the Netherlands*
[12]*Kapteyn Astronomical Institute, PO Box 800, NL-9700 AV Groningen, the Netherlands*
[13]*Sterrenkundig Observatorium, Universiteit Gent, Krijgslaan 281 S9, B-9000 Gent, Belgium*
[14]*Physics Department, Institute for Computational Cosmology, Durham University, South Road, Durham DH1 3LE, UK*
[15]*Physics Department, Centre for Extragalactic Astronomy, Durham University, South Road, Durham DH1 3LE, UK*
[16]*National Astronomical Observatories, Chinese Academy of Sciences, Beijing 100101, People's Republic of China*
[17]*INAF-IRA, Via P. Gobetti 101, I-40129, Italy*
[18]*INAF – Osservatorio Astronomico di Cagliari, Via della Scienza 5, I-09047 Selargius (CA), Italy*
[19]*INAF, Arcetri Astrophysical Observatory, Largo Enrico Fermi 5, I-50125 Florence, Italy*
[20]*Department of Physics, Engineering Physics and Astronomy, Queen's University, Kingston, ON K7L 3N6, Canada*

This paper has been typeset from a TEX/LATEX file prepared by the author.